Master Thesis, Department of Geosciences

Smoke detection in Europe from wildfires in North America and its impact on the surface temperature

Maria Rebecca Roggentin

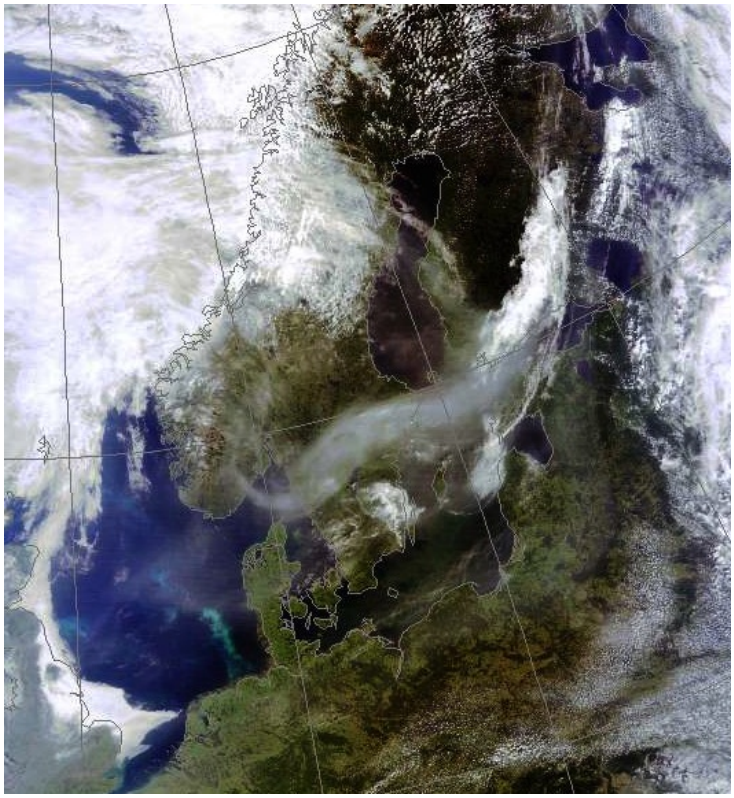

UNIVERSITY OF OSLO

FACULTY OF MATHEMATICS AND NATURAL SCIENCES

Smoke detection in Europe from wildfires in North America and its impact on the surface temperature

Maria Rebecca Roggentin

Master Thesis in Geosciences

Discipline: Meteorology and Oceanography

Department of Geosciences

Faculty of Mathematics and Natural Sciences

University of Oslo

June 13, 2014

ABSTRACT

In the summer of 2013, Europe got affected by smoke from wildfires in North America. A haze was covering the sky, attenuating the incident solar radiation, at many places in Europe. Especially during two periods, high values of Aerosol Optical Depth (AOD) were detected by MODIS over Europe. In omit connection with these periods large aerosol concentrations were observed over the Atlantic, detected by OMPS. Periods concerned are from June 22 to 27 and from July 4 to 14. Research shows that the smoke was most likely due to large fires in Quebec. Sun photometers operated by AERONET showed an AOD of 1.9 in England on June 26 and 1.5 in Sweden on July 8. Ceilometers and LIDAR measurements detected the smoke in Belgium, The Netherlands, Sweden and Norway. All on an altitude of 2-4 km. In the area of interest, research shows that southern part of Norway was influenced by an AOD of approximately 1.1 on July 11 and 12. Simulations by WRF show that an AOD of 1.1 would have affected the surface temperature with 0.25-0.50 degrees. By comparison, an AOD of 10 would have affected the temperature by 1.7-1.9 degrees, which corresponds to a typical value of an altostratus cloud. At such high AOD values temperature effect become non-linear due to saturation effects.

ACKNOWLEDGEMENTS

First of all, I would like to thank my supervisor Jón Egill Kristjánsson for giving me an interesting thesis and excellent guidance during this period. I would also like to thank my co-supervisor Michael Schulz for is suggestions, good explanations and encouragements.

I am further grateful to the PhD candidate Kjetil Schanke Aas for giving me very helpful discussions and being interested in my work. I would also like to thank Anne Claire Fouilloux for showing her programming skills and helping me set up WRF. Bjørg Rognerud has provided me with initial data whenever I need it. I would like to thank her for this work.

I also wish to thank my fellow students for the good social environment in the study room.

Last but not least, my family and friends have always been there for me. Thank you for your support.

CONTENTS

1 INTRODUCTION

A couple of days in the summer of 2013, a haze was covering the sky in Oslo, Norway. This haze was not cloud particles, which could be detected by ceilometer measurements. Similar observations were seen in the rest of Europe for instance by LIDAR measurements in the Netherlands. At Frankfurt and Paris airport, aircrafts measured higher concentrations of carbon monoxide during the same period. Observations were understood to be smoke from wildfires in North America. Figure 1 show a satellite image of the smoke plume, detected over Scandinavia on July 8.

In Oslo, we were suppose to have beautiful summer days, as in clear sky and maximum solar insolation. But this smoke was covering the sun and attenuated the incident radiation. At the institution of Oslo people were discussing about this event and its impact on the surface temperature. The smoke layer, by reflection of solar radiation, could have contributed to a lower surface temperature. This event and discussion were made into a master thesis, which will be presented here. Research questions are: How much did the aerosol layer actually affect the surface temperature? Where did the smoke originate from?

Wildfires occur regularly each summer in North America, which contribute to large areas burned. But in Canada during the summer of 2013, an area of 3.8 million hectare was burned. This was more than three times the 10-yr average. The most affected province was Quebec. It had almost eight times larger area burned than the 20-yr average and more than thirteen times larger than the 10-yr average. The area burned in Quebec was approximately 1.9 million hectares, which is half of the total area burned in Canada that year. [5]

Wildfires are often ignited by lightening and are therefor difficult to control. Smoke, which is emitted by biomass burning, is known as aerosols. Aerosols contribute and respond to climate change, which is well reseacthed by the latest IPCC report [2].

Aerosols in the atmosphere can both contribute to a positive and negative forcing. A positive forcing is a warming of the atmosphere and surface whereby a negative is a cooling. Interaction with aerosols and radiation can be due to scattering and/or absorption by short wave (SW) radiation, referred to *the direct effect*. Scattering by aerosols result in a negative forcing

whereas absorption to a positive. Over all, the direct effect of aerosols is dominated by a negative forcing [15, Hansen et al (2002)]. The direct effect by scattering of the smoke layer observed over Norway will be researched in this thesis. Aerosol particles can also change the radiative properties and lifetime of clouds by acting as an cloud condensation nuclei or ice nuclei [22, Lohmann and Feichter (2005)]. This effect will not be the subject of this paper.

The reflection by an aerosol layer in the atmosphere depends on its optical properties. One of these properties is the Aerosol Optical Depth (AOD). AOD is a measure of the transparency for the solar radiation going threw an aerosol layer. Cited by NASA Earth Observations: "An optical thickness of less than 0.1 indicates a crystal clear sky with maximum visibility, whereas a value of 1 indicates the presence of aerosols so dense that people would have difficulty seeing the Sun, even at mid-day!" [27].

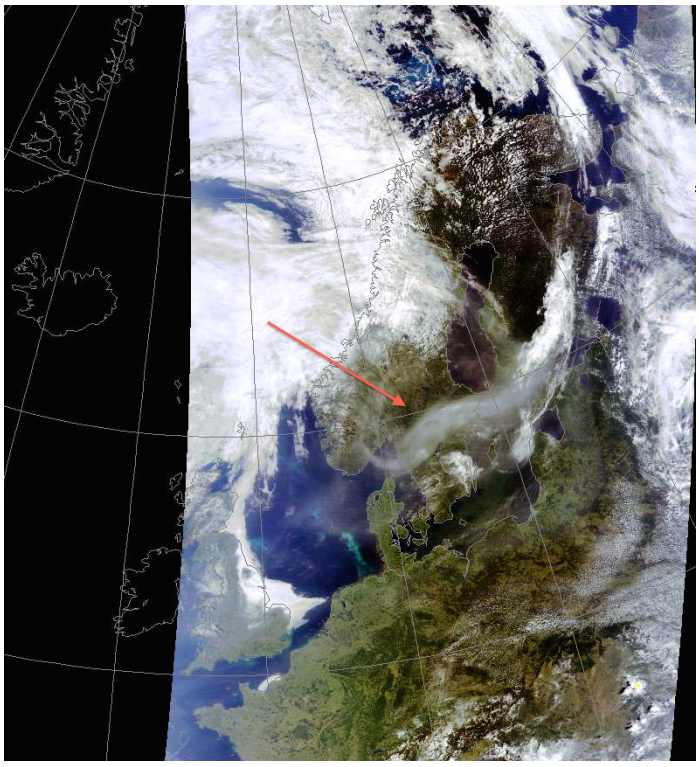

Figure 1: RGB Satellite image on July 8 (2013) by Terra-MODIS. Red arrow points at the smoke plume over Scandinavia. A composite of channels 1 (red, 620-670nm), 4 (green, 545-565nm) and 3 (aqua, 459-479nm), provided by NERC Satellite Receiving Station, Dundee University, Scotland [32].

1.1 ABOUT THIS STUDY

The polar-orbiting satellite instruments Moderate Resolution Spectroradiometer (MODIS) and the Ozone Mapping and Profiler Suite (OMPS) are good tools to detect aerosols globally. Advanced algorithms of the observations by MODIS and OMPS can retrieve the AOD and aerosol index (AI), respectively. AI is a measure of elevated absorbing aerosols by UV radiation. Positive values are mostly connected to aerosols from desert dust and biomass burning.
It is common to sporadically observe high values of AOD over Europe, since it is common in Europe to get influenced by aerosols transported from different parts of the world. By researching the AOD over Europe in the summer of 2013, two periods were seen with high values of AOD for a longer term. It was also seen that Scandinavia reached high values, which is not so typical. For example, detected by MODIS, one pixel exceeded a value of 2.0 over Sweden. This was a pixel surrounded with other high values, see Figure 2 on July 8. Note here, this was the same day as the RGB satellite image in previous section, see Figure 1. It is clearly seen, that the position of the high AOD values observed, had the same position as the reflected particles pointed out with an arrow.
Associated with the two previous discussed periods, high values of AI was seen over the Atlantic, see for example July 7 in Figure 3. From May 1 to September 31, only those two periods had dominated positive values of AI over the Atlantic. The two periods concerned were from June 22 to 27 and July 4 to 14. They will further on be called event 1 and event 2, respectively.

A research about events 1 and 2 is presented in chapter 4. The research is based on various observation systems, for example Ceilometer, MODIS, OMPS, Sun photometer, HYSPLIT and weather analysis. The instruments are described in chapter 3 and the theory behind in chapter 2. Connected to these events a couple of news articles were given, for instance by NASA Earth Observatory and Monotoring atmospheric composition and climate (macc). These will also be discussed.

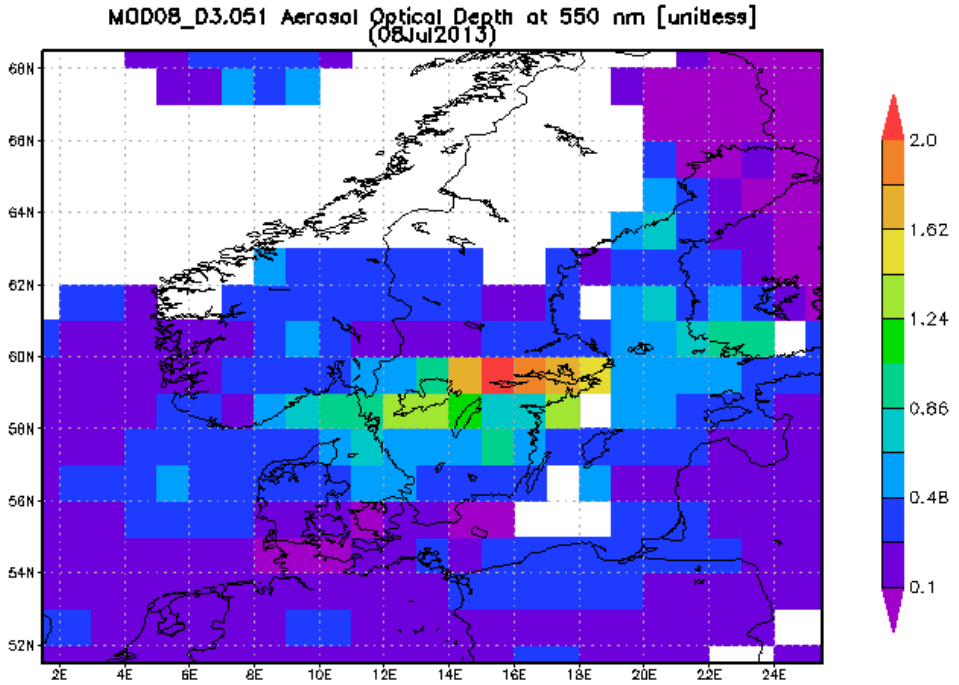

Figure 2: Daily Time-average Lat-Lon Map of Aerosol Optical Depth (AOD) at 550 nm on July 8, 2013, by MODIS-Terra. 1 x 1 degree. Version 5.1. Images downloaded from Giovanni online data system [26].

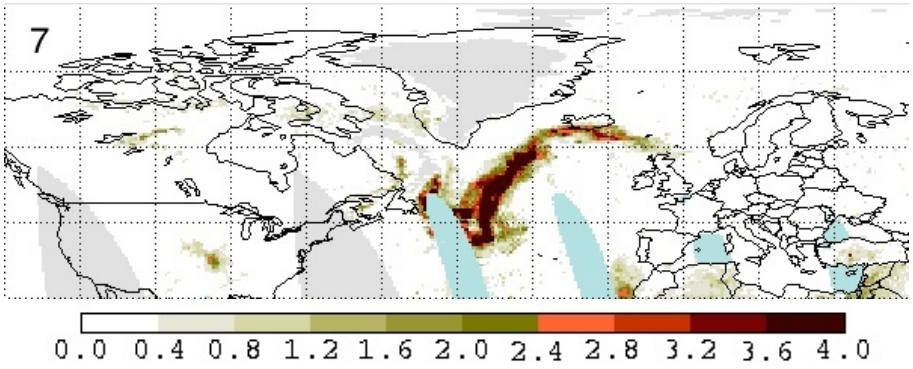

Figure 3: Aerosol Index (AI) Map by OMPS onboard the satellite Suomi-NPP [31].

To research the surface temperature effect of the smoke layer, the Weather Research and Forecasting (WRF) model was used [42, Skamarock et al. (2008)]. In the field of meteorology, WRF is a well-known model and gets used for instance by National Center for Atmospheric Research (NCAR) and National Centers for Environmental Prediction (NCEP). WRF provide availability to different SW radiation schemes to calculate the SW fluxes in the model. SW schemes consider radiation from the solar spectrum being absorbed, reflected and scattered by the surface and the atmosphere. Atmospheric gases and the surface interact with SW radiation and in some

schemes aerosols are taking into account. As the focus in this study is the direct effect of aerosols on SW radiation, a SW radiation scheme treating aerosols was desired. NCAR provides a model called NCAR Community Atmosphere Model (CAM 3.0) [11, Collins et al. (2004)], including a SW radiation scheme optional in WRF. The SW scheme, named CAM shortwave scheme in WRF, take aerosols into account and therefor give the user opportunity to change the aerosol properties.

In this study, the AOD has been changed in the CAM shortwave radiation scheme. The applied method is a One-way nested run using Ndown. The method is described in chapter 5 and results and discussion in chapter 6. Theory behind the CAM shortwave radiation scheme is described in chapter 2.

A conclusion of the research on the two events and results of the simulations by WRF are presented in chapter 7.

2

THEORY

The definition of an atmospheric aerosol is: a suspension of a fine solid or liquid particle in a gas [41]. The particle is usually surrounded with air and has a terminal fall speed close to zero [45].

2.1 RADIATIVE EFFECTS OF AEROSOLS: THE DIRECT EFFECT

The direct effect is when solar radiation gets scattered or/and absorbed by aerosol particles. The reflection and absorption by an aerosol layer of the atmosphere depends on its optical properties, that is: The Aerosol Optical Depth (AOD), τ_{aer}, single scattering albedo, ω_{aer}, and the asymmetry parameter, g_{aer} [21].

2.1.1 *Aerosol Optical Depth*

The size spectrum of particles can be described by n(a) [$m^{-3}\mu m^{-1}$]. The total number of particles per unit volume [1 m^{-3}] is given by

$$N = \int_{a_1}^{a_2} n(a)da \tag{1}$$

where a_1 to a_2 [μm] is the assumed size range of particles. The scattering and absorption coefficient [m^{-1}], β_{sca} and β_{abs}, respectively, is defined

$$\beta_{sca,abs} = \int_{a_1}^{a_2} \sigma(a)_{sca,abs} n(a)da \tag{2}$$

where σ_{sca} and σ_{abs} is the scattering and absorption cross section [m^2], respectively. The coefficients depend on the wavelength, λ, of the incident radiation. The extinction coefficient is given by

$$\beta(\lambda)_{ext} = \beta(\lambda)_{abs} + \beta(\lambda)_{sca} \tag{3}$$

The Optical Depth τ [unitless], also called Optical Thickness, is the extinction coefficient integrated from an altitude z_0 to z [m], defined as

$$\tau(\lambda) = \int_{z_0}^{z} \beta(\lambda)_{ext} dz \tag{4}$$

By the extinction coefficient of aerosols, the AOD can be retrieved, given as

$$\tau(\lambda)_{aer} = \int_{z_0}^{z} \beta(\lambda)_{ext,aer} dz \tag{5}$$

2.1.2 *Single-Scattering Albedo*

The so-called single-scattering albedo, ω, is a measure of how much light a particle is influenced by scattering relative to the total amount attained by extinction. With equation 2 by scattering and equation 3, single-scattering albedo of aerosols is defined

$$\omega(\lambda)_{aer} = \frac{\beta(\lambda)_{sca,aer}}{\beta(\lambda)_{ext,aer}} \tag{6}$$

2.1.3 *Asymmetry Parameter*

The asymmetry parameter is defined

$$g(\lambda) = \frac{1}{2}\int_{-1}^{1} P(\cos\theta')\cos\theta' d\cos\theta' \tag{7}$$

where θ' is the angle between the incident radiation and the scattered radiation. The so-called scattering phase function, $P(\cos\theta')$, is the probability that photons are scattered in the forward direction. The asymmetry factor range from -1 to 1. When g=1 it is completely forward scattering and when g=-1 it is backward scattering. For isotropic scattering, the asymmetry factor is zero.

2.2 PRINCIPLE OF SUN PHOTOMETER

2.2.1 *Aerosol Optical Depth Retrievement*

The incoming intensity from the sun is proportional to $I \propto \frac{1}{r^2}$. This in combination with Beer-Bouguer-Lambert law can be written

$$I(\lambda) = \frac{r^2}{{r_0}^2} I(\lambda_\infty)\, e^{-\tau(\lambda)\, m(\theta)} \tag{8}$$

where

$I(\lambda)$: monochromatic intensity [W $m^{-2}sr^{-1}$]
$I(\lambda_\infty)$: monochromatic intensity at top of the atmosphere [W $m^{-2}sr^{-1}$]
r : actual sun-earth distance [m]
r_0 : mean sun-earth distance [m]

and the air mass factor is $m(\theta) = \frac{1}{\cos(\theta_0)}$, where θ_0 is the solar zenith angle. By sun photometer measurements of $I(\lambda)$ and an assumption of $I(\lambda\infty)$, the total optical depth in equation 8 can be obtained. The optical depth consist of different wavelength-dependent components and they need to be subtracted to get the Aerosol Optical Depth [24]

$$\tau(\lambda)_{aer} = \tau(\lambda) - \tau(\lambda)_W - \tau(\lambda)_{Ray} - \tau(\lambda)_{O_3} - \tau(\lambda)_{NO_2} - \tau(\lambda)_{CO_2} - \tau(\lambda)_{CH_4} \quad (9)$$

where W=water vapor, Ray=Rayleigh and the other components are gases, which are based on assumptions.

2.2.2 *Fine Mode Fraction*

The Ångström exponent is defined as the first derivative of AOD due to wavelength in logarithmic scale:

$$\alpha = -\frac{d\ln\tau_{aer}}{d\ln\lambda} \quad (10)$$

The Ångström exponent can be calculated using two or more wavelengths and a least square fit. Particle sizes can be described in two modes; fine mode with particles less than $1\mu m$ and coarse mode with particles greater than $1\mu m$. The aerosol optical depth of fine mode particles are highly sensitive to visible wavelengths ($0.5\mu m$) and coarse mode particle to near infrared wavelengths ($1\mu m$) By using equation 10 with wavelengths of visible and near infrared, the Ångstrom exponent can be calculated, containing information of the combined size contributions of fine and coarse aerosols. While using wavelengths in the visible Ångstrom exponent can be calculated for fine mode particles. With the two values and their spectral derivative the fine aerosol depth can be calculated, τ_f, and then the coarse optical depth is given by [34]

$$\tau_c = \tau_{aer} - \tau_f \quad (11)$$

The fine mode fraction is then defined

$$\eta = \frac{\tau_f}{\tau_a} \quad (12)$$

2.3 PRINCIPLE OF LIDAR

The **L**ight **D**etection **A**nd **R**anging (LIDAR) is an active remote sensing instrument. A laser send out short pulses of high power and the backscattered signal is measured. By the receieved backscattering signal, the comosition and structure of clouds, aerosols and minor gases in the atmosphere can be detected.

The the basic LIDAR equation is expressed [21]

$$\bar{P}_r(r) = \frac{P_t C A_r \beta_\pi(r) \Delta h}{8\pi r^2} \exp\left(-2\int_0^r \beta_e(r')dr'\right) \tag{13}$$

where

C	: an instrument factor
P_t	: transmitted power [W]
A_r	: receiver aperture [m^2]
Δh	: pulse length transmitted [m]
r	: distance from LIDAR (height) as a function of time [m]
$\beta_\pi(r)$	: volume backscattering coefficient as a function of height [1/m]
$\beta_e(r)$	: volume extinction coefficient as a function of height [1/m]

C, P_t, A_r, Δh and r are known parameters. β_π and β_e are related to the optical properties and are unknown. To distinguish between molecular scattering (Rayleigh scattering) and particle scattering (aerosol and clouds scattering), these parameters are divided up: $\beta_{\pi,Ray}/\beta_{e,Ray}$ for Rayleigh backscattering/extinction and $\beta_{\pi,aer}/\beta_{e,aer}$ for aerosol backscattering/extinction. With measured or assumed vertical profiles of temperature and pressure in the atmosphere, the Rayleigh coefficients, $\beta_{\pi,Ray}$ and $\beta_{e,Ray}$, can be found [18]. In general, a relationship between the backscatter and extinction coefficient for aerosol particles is given by

$$L = \frac{\beta_{e,aer}}{\beta_{\pi,aer}} \tag{14}$$

Reasonable approximation has been found, assuming spherical particles (Mie theory), that L=0.6525. This value has been used in many cases. [21]
If equation 13 is multiplied with r^2, the range dependence will be removed and the so-called range-corrected signals can be obtained. The range-corrected signal is making the backscattering of particles be largely dominant.

2.4 SATELLITE REMOTE SENSING OF AEROSOLS

The technique of instruments on satellites is (in most case) that they measure the received radiation reflected by the atmosphere and surface, called

passive remote sensing. From the upscattered (reflected) radiation, aerosol properties can be derived.
The received radiation at each wavelength can be formed into spectral reflectance, $\rho_{TOA}(\lambda)$. The reflectance get contribution from aerosol scattering, $\rho_{aer}(\lambda)$, Rayleigh scattering, $\rho_{Ray}(\lambda)$, and surface albedo, $\rho_{sfc}(\lambda)$, while assuming a optically thin atmosphere. The assumption is the explanation why AOD can not be retrieved during cloudy conditions. To receive the aerosol reflectance the other contributed reflectances need to be subtracted from the measured reflectance. Taking into account the bidirectional reflectance from the atmosphere-surface system the aerosol reflectance is given by [21]

$$\rho_{aer}(\lambda) = \rho_{TOA}(\lambda) - \rho_{Ray}(\lambda) + \frac{\rho_{sfc}(\lambda)}{1 - \rho_{src}(\lambda)\rho_{Hem}} T(\lambda) \tag{15}$$

where $T(\lambda)$ is the total transmission, including direct and diffuse transmission, and ρ_{Hem} is the spherical albedo of the atmosphere. The total transmittance is given by the radiative transfer equations. The spherical albedo gets less important over low reflecting surfaces and parameterization can be done. By knowing the spectral dependence of Rayleigh optical depth and phase function, the Rayleigh reflectance can be calculated. With the known variables, the spectral aerosol reflectance in equation 15 can be computed and the AOD can be derived, assuming their phase function and single-scattering albedo. Complicated algorithms is used for MODIS and described in [20, Levy et al. (2010)].

2.5 AEROSOL INDEX

Aerosol Index (AI) is an value which indicate the presence of absorbing aerosols by UV radiation in the atmosphere. The index is calculated from observations (instrument on satellites) and models. The basic idea is to calculate non absorbing spectral radiance ratios by models and subtract that value from the spectral radiance ratios observed. The spectral radiance ratios is the spectral contrast between two wavelengths in the UV region, where ozone absorption is small. AI is defined as [25]

$$AI = 100\,[\,\log_{10}(I_{\lambda_1}/I_{\lambda_2})_{measured} - \log_{10}(I_{\lambda_1}/I_{\lambda_2})_{calculated}\,] \tag{16}$$

where I is the measured and calculated (models) spectral radiance for typically wavelengths of λ_1=360 nm and λ_1=331 nm. A positive AI represents UV absorbing aerosols, like smoke and dust, a negative value represents non UV absorbing aerosols and clouds.

2.6 WILDFIRES

Emissions to the atmosphere from wildland fires consist of a wide variety gases and particulate matter, such as the greenhouse gases carbon dioxide (CO_2), methane (CH_4), nitrous oxide (N_2O), photochemically reactive compounds carbon monoxide (CO), nonmethane volatile organic carbon (NMVOC), nitrogen oxides (NOx) and fine and coarse particulate matter. The emissions depend on vegetation type and flaming or smoldering combustion. [44]
The particle sizes in emissions from biomass burning can be described by different modes: nucleation mode, accumulation mode and coarse mode. Accumulations mode is the dominated one and has a size range of 0.1-0.15µm. Accumulation mode consist of organic matter, black carbon and inorganic materials. When smoke is freshly emitted it is usually in the nucleation mode with diameters <0.03µm. Small timescales, a few minutes to a half a hour after emission, coagulation takes place, and particles in the nucleation mode transfer into the accumulation mode. [16, Janhäll et al. (2010)] Typical sizes of coarse mode particles is 2.5 µm-15 µm and stands for 10% of the accumulation mode particles. The accumulation mode particles consist mainly of organic carbon (~50-60%) and a small amount of black carbon (~5-10%). [37, Reid et al. (2005)] Organic carbon and black carbon can last in the troposphere for approximately 1 week, when they further on get removed by wet or dry deposition. Different properties of the aerosols make the organic carbon interact mainly by scattering of solar radiation and black carbon through absorption. [2]

2.7 CAM SHORTWAVE SCHEME

CAM shortwave scheme [11, Collins et al. (2004)] is treating each column independently, so-called one-dimensional scheme. This is the same approach for all radiation schemes in WRF. Fluxes are computed for every infinite horizontally uniform layer, where the sum of the fluxes provides the atmospheric heating. Short wave and long wave heating rates are computed every hour.
The solar spectrum is divided into 19 discrete spectral intervals, ranging from 0.2 to 5 µm. Different bands take care of different extinction properties by gases and aerosols. The greenhouse gases ozone, water vapor and carbon dioxide, stands for seventeen bands and one is for visible radiation and one for near-infrared. The visible band range from 0.35 to 0.64 µm. Calculations of shortwave formulations are made by δ-Eddington approximation [3, Briegleb, B. P. (1992)].

2.7.1 *δ-Eddington approximation in CAM*

The atmosphere in the model is divided into a number of vertical layers. For each model grid point, every layer is assumed to be horizontallly and vertically homogeneous. On the layer interface, the upward and downward fluxes are computed for each spectral band. Every homogeneous layer will absorb and/or scatter radiation. Absorption and scattering by the layer are due extinction optical depth, see equation 9, single scattering albedo, see equation 6, asymmetry parameter, see equation 7, and forward scattering fraction. These bulk layer properties for each grid box, are defined by [9, Cess, R.D. (1985)]

$$\tau = \sum_i \tau_i \tag{17}$$

$$\omega = \frac{\sum_i \omega_i \tau_i}{\tau} \tag{18}$$

$$g = \frac{\sum_i g_i \omega_i \tau_i}{\omega \tau} \tag{19}$$

$$f = \frac{\sum_i f_i \omega_i \tau_i}{\omega \tau} \tag{20}$$

Scattering of radiation by atmospheric particles is in general highly peaked in the forward direction. The Eddington approximation for highly asymmetric phase functions is not accurate and therefor the forward peak of the phase function need to be approximated as a δ-function. This leads to an adjusted extinction optical depth, single scattering albedo and asymmetry factor, defined

$$\tau^* = \tau(1 - \omega f) \tag{21}$$

$$\omega^* = \omega \left(\frac{1 - f}{1 - \omega f} \right) \tag{22}$$

$$g^* = \frac{g - f}{1 - f} \tag{23}$$

With adjusted properties, the reflectivity and transmissivity due to direct radiation and diffuse radiation at a cosine zenith angle can be calculated for

each layer, for details see [10, Coakley et al. (1983)]. The layers are then combined assuming radiation scattered once, is diffuse. The interface between each layer is combined and at every interface reflectivities and transmissivities are available. With these values the upward and downward flux at each interface can be computed. The upward and downward fluxes are summed for every spectral interval, called spectrally integrated fluxes. The upward and downward spectrally integrated fluxes are differenced to maintain the heating rate.

3 INSTRUMENTS

To detect the smoke plumes over Europe, various observation systems were used. This chapter will describe different observation system and data access.

3.1 CEILOMETER AT OSLO-BLINDERN

Ceilometer Jenoptik CHM15K, located on the roof of Meteorologisk Institutt at Blindern/Oslo, Norway, provides information about atmospheric aerosols and droplets. It measures for instance cloud base height for 3 layers and aerosol backscatter profiles. The measuring range goes up to 15 000 meter. Using the principle of LIDAR, described in chapter 2 under section 2.3, the instrument can detect particles by the backscattered laser light. [17] Data from the ceilometer at Meteorologisk Institutt was downloaded at *ftp://ftp.met.no/users/ceilometer*, access provided from the co-supervisor of this thesis, Michael Schulz. Ceilometer data for aerosol backscatter profiles and cloud base height was computed with Matlab.

3.2 AERONET

The **AE**rosol **R**obotic **NET**work (AERONET) is an aerosol network based on ground-based remote sensing, see chapter 2 under section 2.2. AERONET is established by NASA and PHOtométrie pour le Traitement Opérationnel de Normalisation Satellitaire (PHOTONS) in a partnership with variety universities, institutes and national agencies worldwide. Data are available, among other parameters, for the AOD, Ångstrom parameter and Fine Mode Fraction. Different levels describe the quality of the data: Level 1.0, Level 1.5 and Level 2.0. Level 2.0 has the best quality. It is cloud-screened and quality assured. Level 1.5 and Level 1.0, is cloud-screened and unscreened, respectively. [24]

3.3 MODIS

Moderate **R**esolution **I**maging **S**pectroradiometer (MODIS) is an instrument, using the technique of passive remote sensing of aerosols, see chapter 2 under section 2.4 for theory behind. The instrument is carried by the polar-orbiting satellites Terra and Aqua, which are included in NASA's Earth Observing System (EOS). Terra is passing the equator, from north to south, at

10:30 a.m and Aqua is passing, from south to north, at 1:30 p.m. Terra and Aqua cover the Earth in 1 to 2 days.
MODIS receives radiation at wavelengths ranging from 0.4 μm to 14.2 μm. Seven bands can retrieve aerosol information. The channels are 1, 2, 3, 4, 5, 6 and 7, named as 0.66, 0.86, 0.47, 0.55, 1.24, 1.64 and 2.12 μm channels, respectively.
MODIS on Terra and Aqua has advantages and disadvantages. Terra and Aqua, because of their polar orbit, can not provide continuous viewing of one location, which can be done by geostationary satellites. On the other hand, the polar-orbiting satellites give higher resolution and can also detect on higher latitudes. According to [38, Remer et al. (2005)], the MODIS aerosol optical depth product has an uncertainty of $\Delta\tau \pm 0.03 \pm 0.05\tau$ over ocean and $\Delta\tau \pm 0.05 \pm 0.15\tau$ over land, validated with two years of AERONET data. MODIS also has impossibilities of detecting AOD under a cloud cover and sometimes AOD pixels are misidentified with cloud pixels. In the end, despite disadvantages, the AOD product is a good tool for detecting aerosols globally over land and ocean.
The images used in this study are the "Aerosol Optical Depth at 550 nm" by MODIS Aqua and Terra version 5.1. The images were produced with Giovanni online data system [26], developed and maintained by the NASA Goddard Earth Sciences Data and Information Services Center (GES DISC) [1]. It is a daily global 1 x 1 degree product, which in this case a Lat-Lon map has been used.

3.4 HYSPLIT

Hybrid **S**ingle **P**article **L**agrangian **I**ntegrated **T**rajectory (HYSPLIT) Model is an web-based tool, provided by NOAA Air Resources Laboratory. The model can compute forward and backward trajectory of an air parcel. In this study, back trajectories from event 1 and 2 are computed from defined altitudes in Europe. [12]

3.5 OMPS

The Ozone Mapping and Profiler Suite (OMPS) is an instrument flying onboard the Suomi National Polar-orbiting Partnership (Suomi-NPP) satellite, established by NASA. The instrument is a back-scattered UV radiation sensor. The parameter used in this study is the Aerosol Index, which is based on the theory in chapter 2 under section 2.5. [31]
The Aerosol Index (AI) has sensitive to the amount, size distribution and height of the absorbing aerosols [43, Torres et al. (1998)].

3.6 CALIOP

Cloud-Aerosol Lidar with Orthogonal Polarization (CALIOP) is an nadir-viewing instrument flying on Cloud-Aerosol Lidar and Infrared Pathfinder Satellite Observations (CALIPSO) satellite, established by NASA and the French space agency, CNES. CALIOP uses the principle of LIDAR, see chapter 2 under section 2.3. The laser beam transmitted (1064 nm and 532 nm) is linearly polarized. The receiver is sensitive to polarization, which can retrieve the degree of linear polarization. CALIOP provide aerosol and cloud profiles and is especially useful in the presence of high thin clouds and high aerosol layers. [46, Winker et al. (2007)]

4

WILDFIRE RESEARCH AND SMOKE DETECTION OVER EUROPE

This chapter will research event 1 and event 2. Recall, event 1 is from June 22 to 27 and event 2 from July 4 to July 14, 2013.

4.1 EVENT 1: SMOKE DETECTION OVER EUROPE

MODIS observations for AOD at 550nm showed that on June 25 two pixels exceeded a value of 4.6 south of England. The pixels were surrounded with values higher than 2, see Figure 4a. The following day, see Figure 4b, there are still high values of AOD in the area. Centered over England, values are approximately 1, with one pixel of 1.9 on the west coast of France. The image on June 27 is not shown in this paper, but is similar to the image on June 26, but more centered over the boundary between France and Spain.

AERONET observations by sun photometer showed an AOD of 1.9 at 500nm at the cite Wytham Woods on June 26. Wytham Woods is located 5 km northwest of Oxford in England (51N,1W). At the cite Coruna, on the west coast of Spain (43N,8W), an AOD value of approximately 0.8 at 500nm was detected on June 27. Both AOD observations are level 2.0 data, which are cloud-screened and quality assured. [24]

Ceilometer at Uccle, Neatherlands, detected smoke particles on June 26, see Figure 5. The smoke plume was located on an altitude of 3.5 km and had a thickness of approximately 500m. [39].

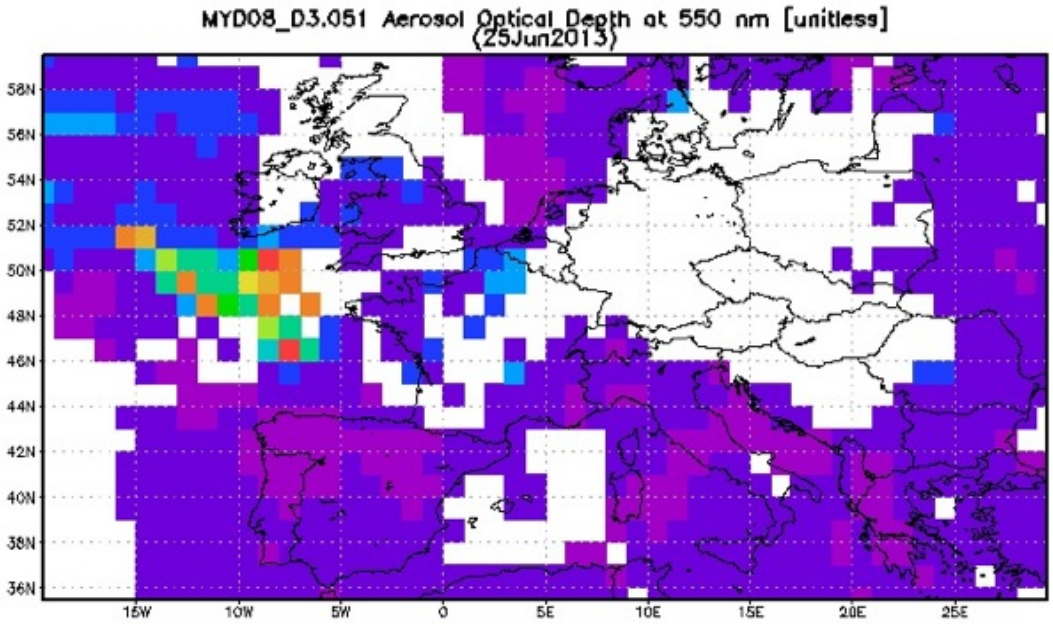

(a)

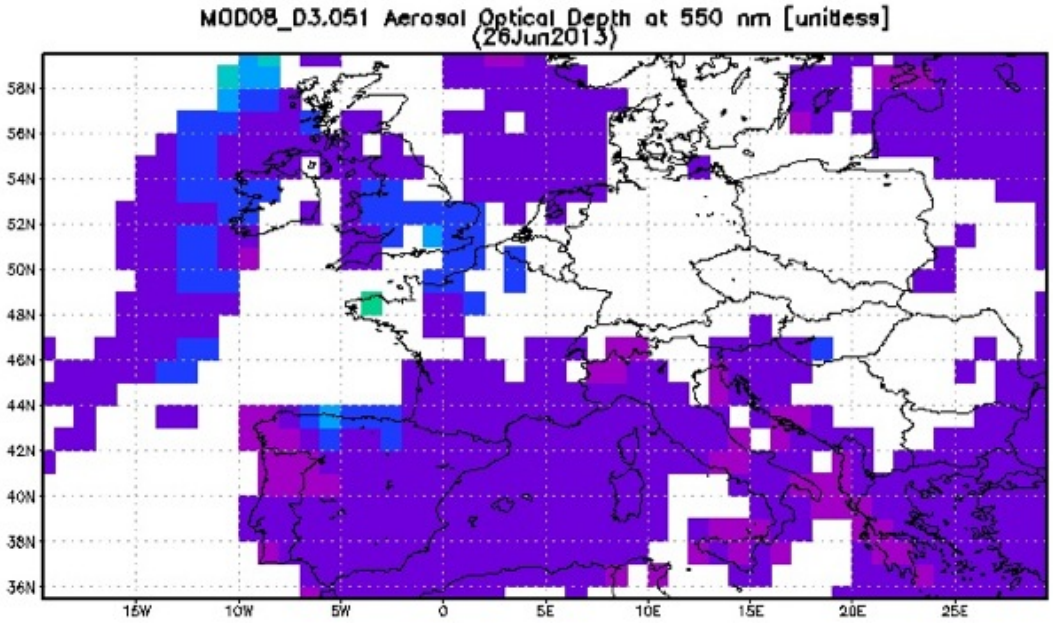

(b)

Figure 4: Daily Time-average Lat-Lon Map of Aerosol Optical Depth (AOD) at 550 nm on June 25 (a), by MODIS-Aqua, and June 26 (b), MODIS-Terra. Both from year 2013. 1 x 1 degree. Version 5.1. Images downloaded from Giovanni online data system [26].

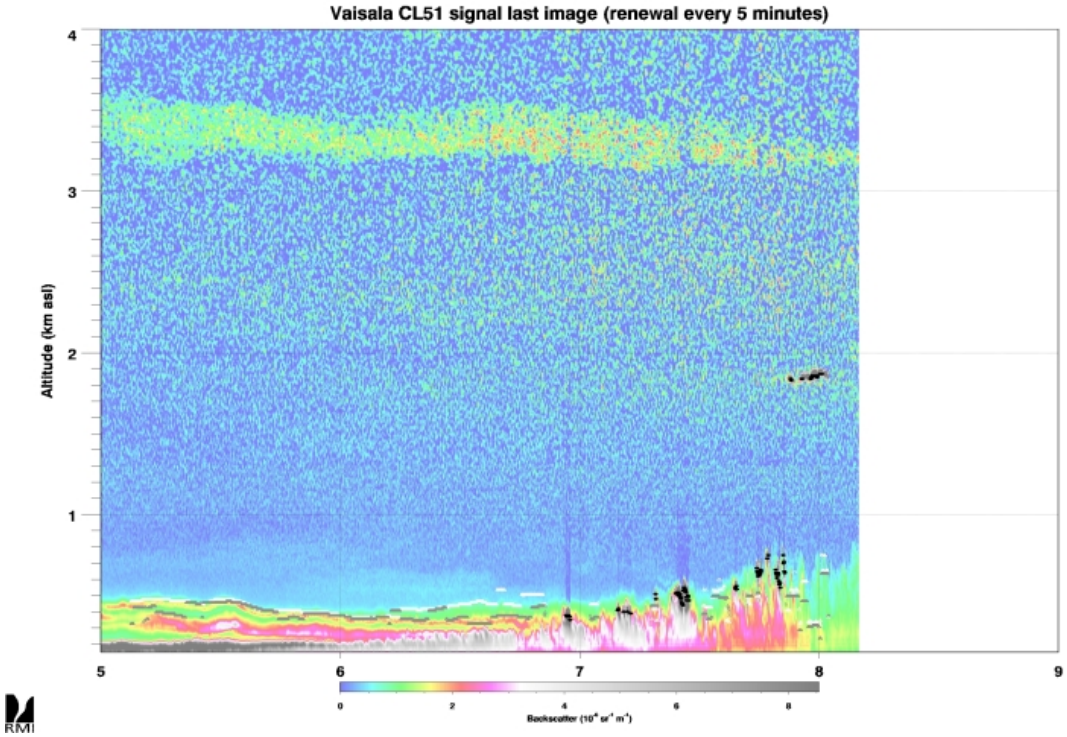

Figure 5: Ceilometer measurements of backscatter on June 26 in Uccle, Neatherlands, by The Royal Meteorological Institute of Belgium (RMI) [39].

4.2 EVENT 1: WILDFIRE RESEARCH

OMPS observations for AI show a concentrated aerosol plume over the Atlantic just two days before the smoke reached south of England (June 25), see AI in Figure 6 for June 23 (a), 24 (b) and 25 (c). On June 25, aerosols south of England are on the same position as the high values of AOD detected by MODIS, see previous Figure 4a. AI is sensitive to height and aerosol concentration, which indicates that the aerosols was on a high altitude and had large concentrations when traveling over the Atlantic.

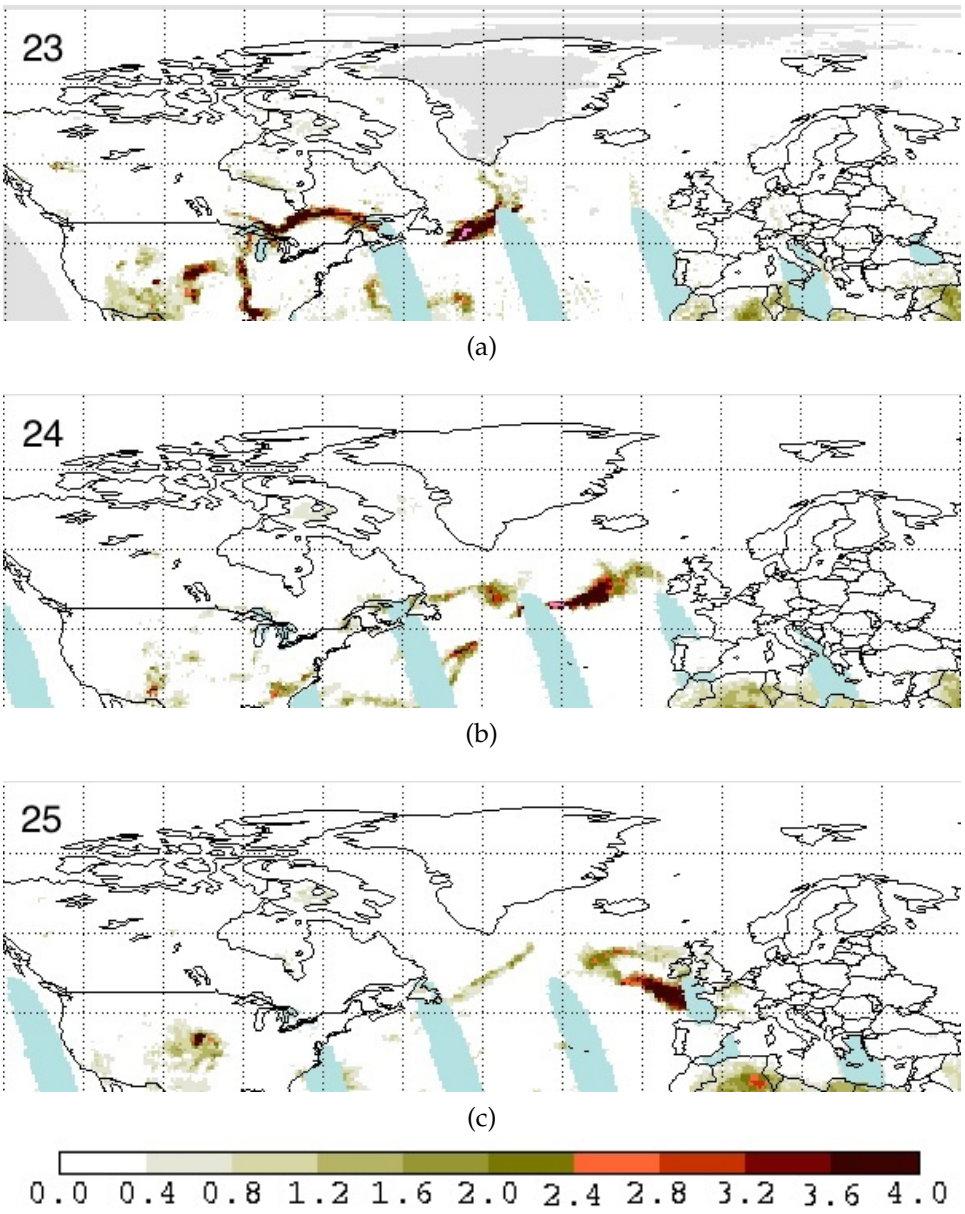

Figure 6: OMPS Aerosol Index (AI) Maps on June 23 (a), June 24 (b) and June 25 (c), by the satellite Suomi-NPP. All from year 2013. [31]

That smoke from North America reached Europe on June 25 is discussed in a couple of news articles, for example by NASA Earth Observatory.

NASA Earth Observatory describe that the main source of the smoke transportation over the Atlantic was Quebec (Canada) but may have had contribution from wildfires in Colorado (U.S) [29]. The Royal Netherlands Meteorological Institute (KNMI), on the other hand, describe only that the smoke originated from wildfires in Colorado, in the Rio Grande National Forest around West Fork. The fire ignited by lightening on June 5 and increased rapidly because of strong winds on June 20. [19] The research by KNMI

was based on satellite measurements of AI. As can be seen for AI measurements on June 23, see previous Figure 6a, the satellite detected one smoke plume east of Newfoundland (south of Greenland) and one south of James bay (west of New York). The smoke in the center of U.S is the wildfires in Colorado. The smoke plume east of Newfoundland was of most likely the one reaching Europe, according to the same structure and the continuity of movement eastward on the next two days (see the next two days 6b and 6c). The smoke plume south of James Bay has a banana shape. In the weather situation of the geopotential height at 500mb, see Figure 7, the shape of the isohyps are similar to the shape of the smoke plume. The winds follow the isohyps and they are leading back to Colorado (center of U.S), where windspeed of 50 knot is observed. It is therefor understandable to think that colorado is the source of both smoke plumes. As we will see, this was probably not the case.

The smoke tracking described in NASA Earth Observatory was based on a forward trajectory analysis by the meteorologist Alain Malo at the Meteorological Service of Canada [29]. Figure 8 show the mass loading on June 23, at 01:00 UTC (a) (1 hour after start) and at 20:00 UTC (b). Figure 9 show for June 25, at 17:00 UTC. The source was east of Manicouagan Lake (Quebec). The round circle west of the source in Figure 8a is the Manicouagan Lake. As can be seen in Figure 8b on June 23, the position and structure of the smoke plume is in a goos agreement with the observations detected by OMPS, see previous Figure 6a. As well as the position of the smoke plume south of England, compare Figure 6c and 9.

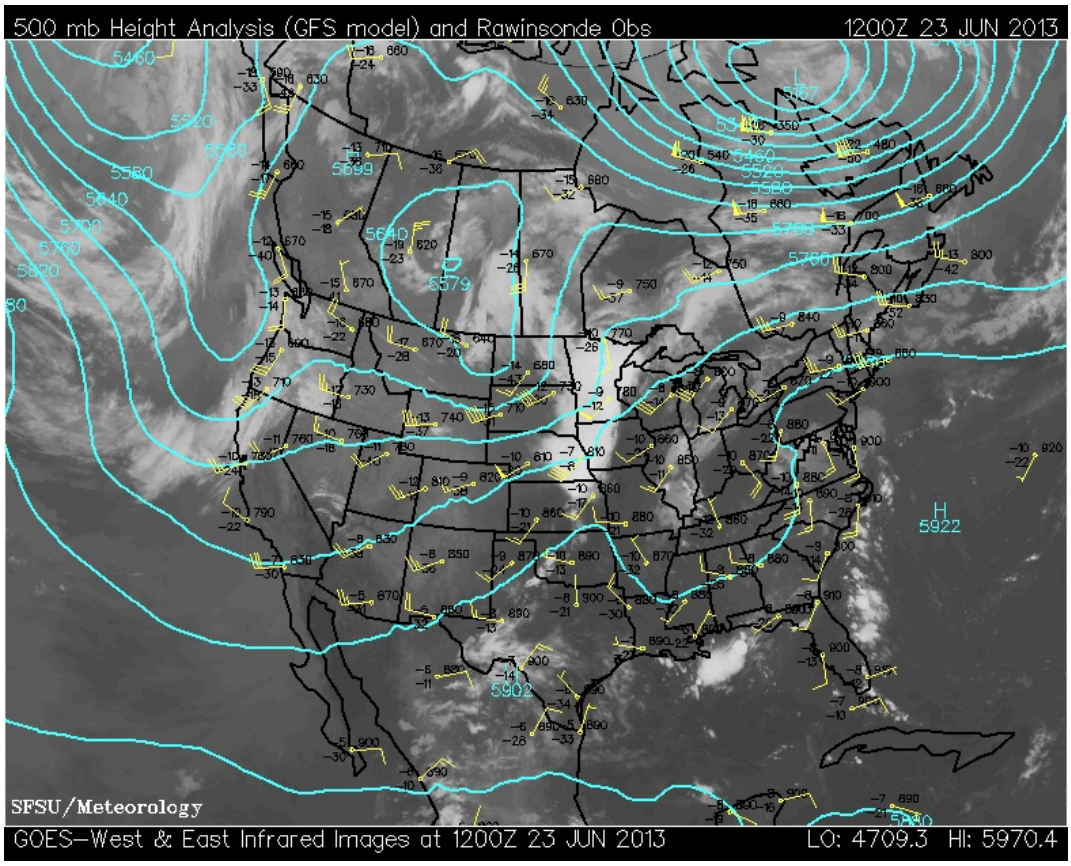

Figure 7: 500 mb Height Analysis (GFS model) and Rawinsonde Obs on June 23 at 1200 Z, 2013. Satellite infrared image is from GOES-West & East. [4]

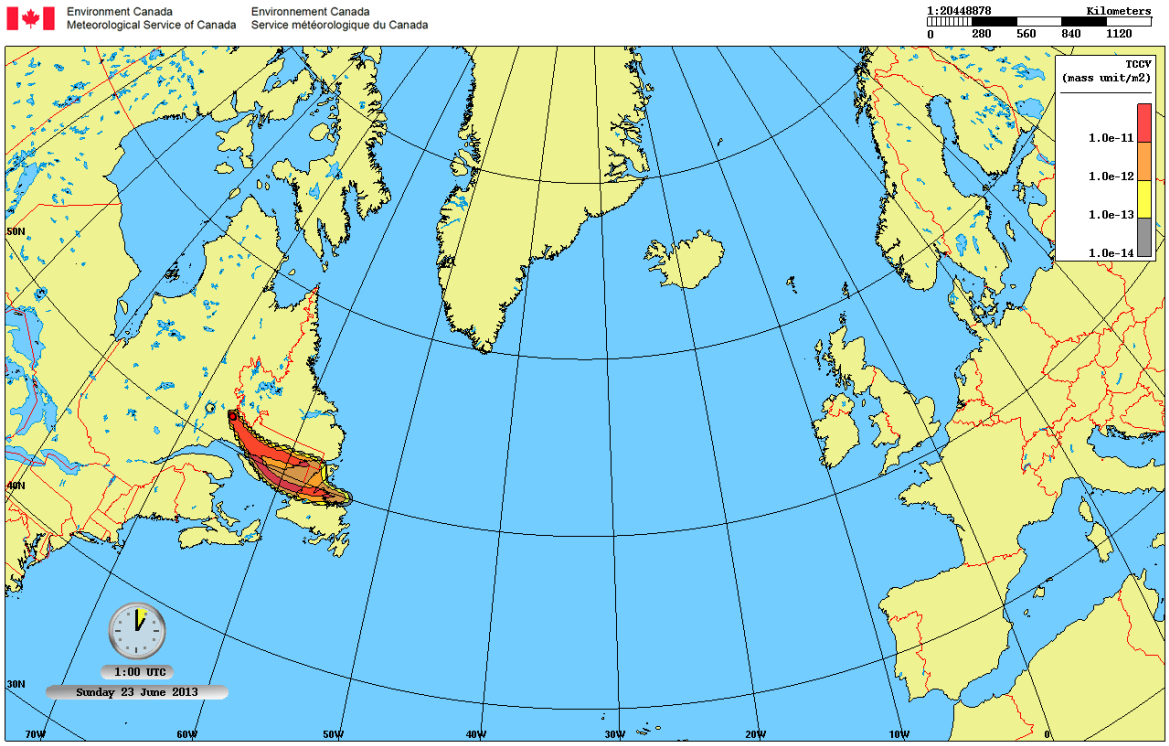

(a)

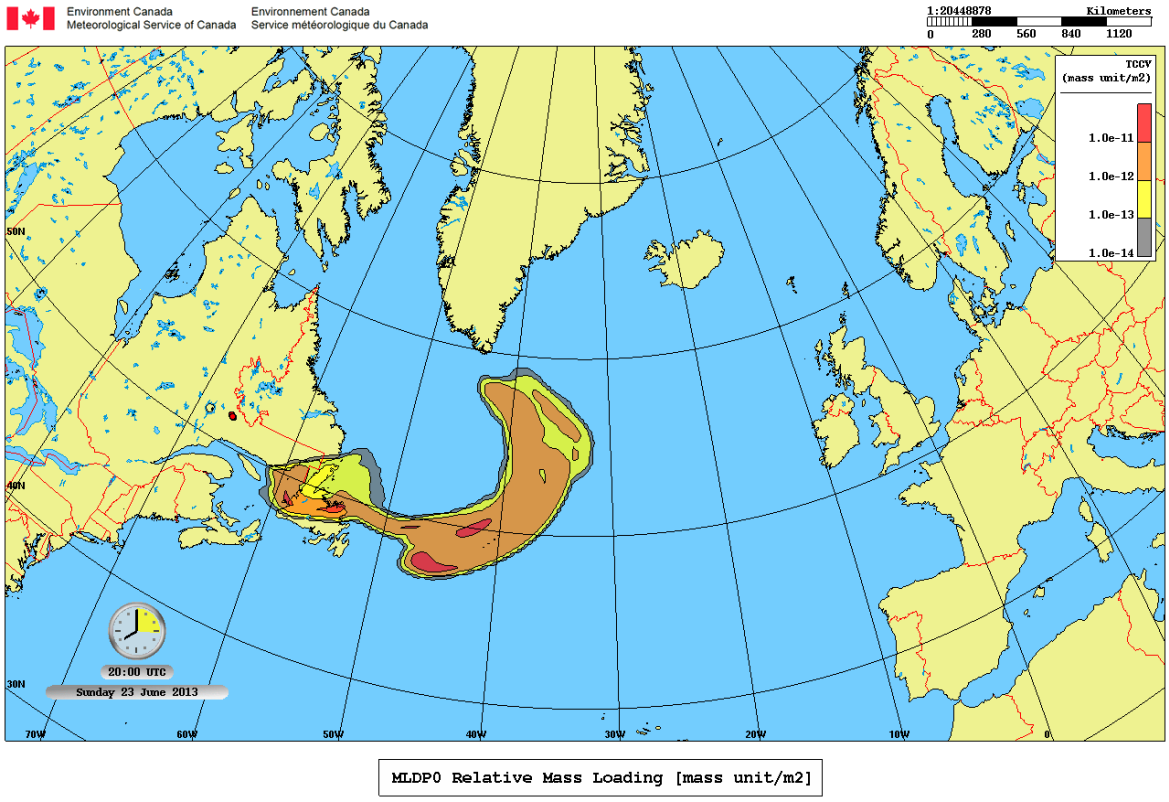

(b)

Figure 8: Forward trajectory analysis for relative mass loading [mass unit/m^2] on June 23 at 01:00 UTC (a) (1 hour after start) and at 20:00 UTC (b). Start of trajectory on June 23 at 00:00 UTC, source east of Manicouagan Lake in Quebec, Canada. [29]

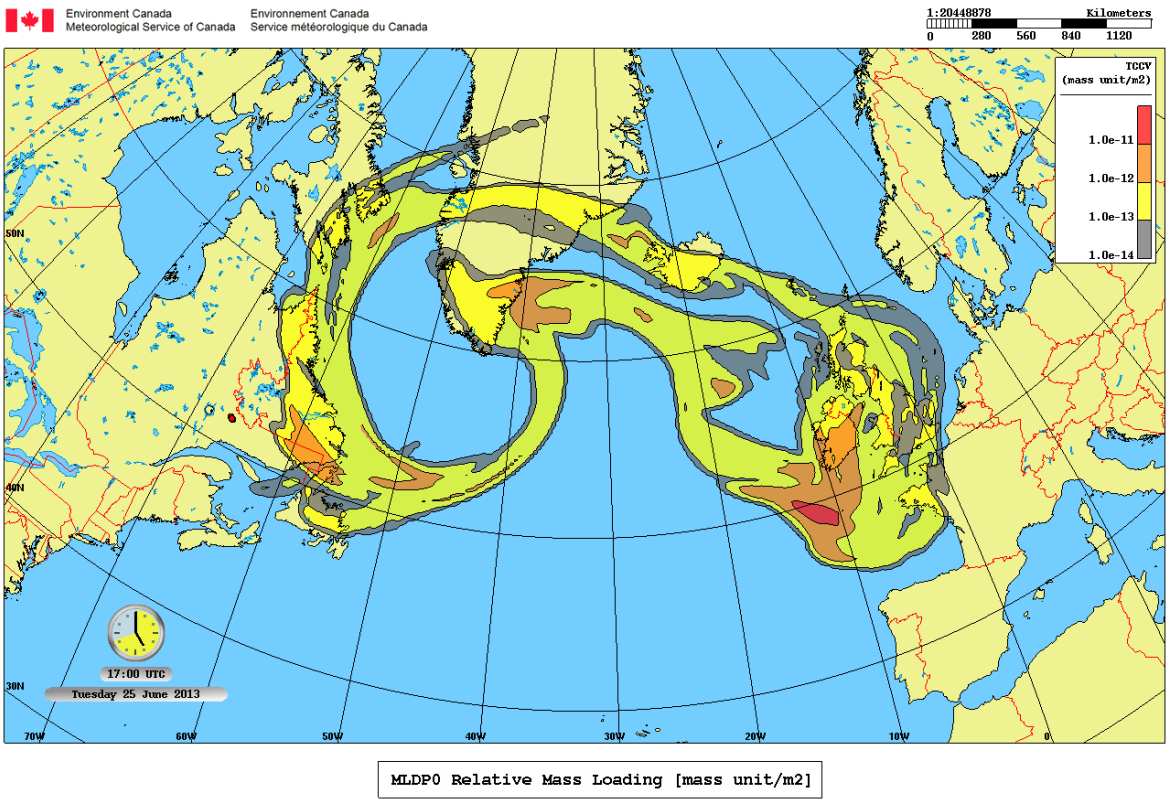

Figure 9: Forward trajectory analysis for relative mass loading [mass unit/m^2] on June 25 at 17:00 UTC. Start of trajectory on June 23 at 00:00 UTC, source east of Manicouagan Lake in Quebec, Canada. [29]

As the smoke plume in Europe was detected on an altitude of 4 km, see previous section 4.1 in Figure 5, a back trajectory by HYSPLIT can be made, see figure 10. The back trajectory indicates further again that the air mass originated from east of New Foundland and further over Quebec.

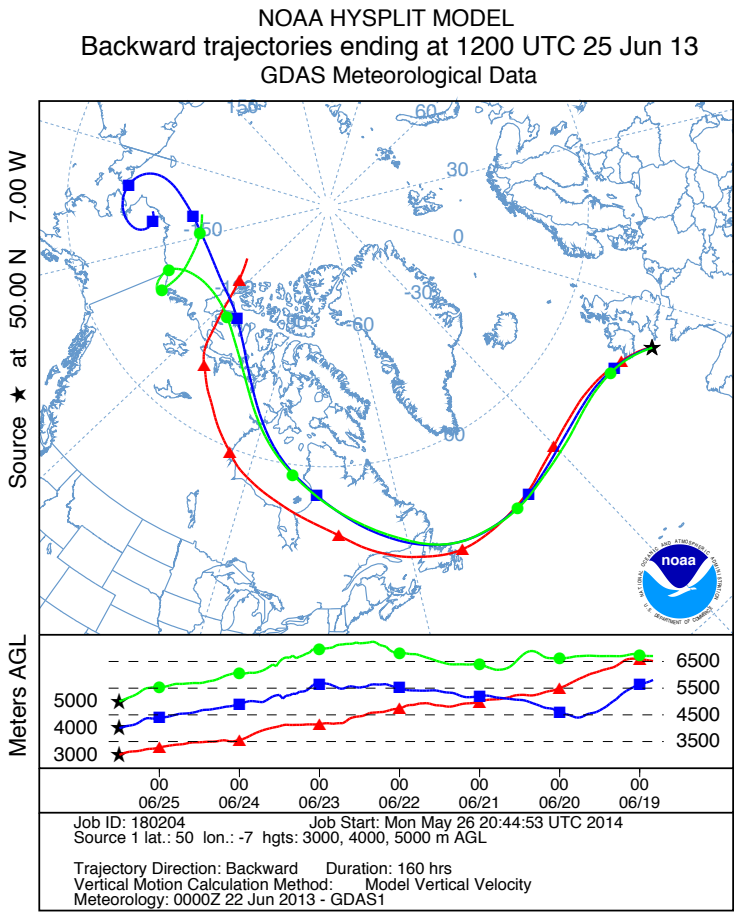

Figure 10: NOAA HYSPLIT model. Back trajectories from south of England, starting on June 25 at 12 UTC, 2013. Starting altitudes are: 3000 km (red), 4000 km (blue) and 5000 km (green). [12]

The Canadian Wildland Fire Information system announced on June 26 an weekly area burned in Canada of approximately 500 000 ha, which was twice the 10 yr average that week. The large area burned was due to large wildfires in Quebec, which accounted for 92 %. [7]

PyroCb, by Cooperative Institute for Meteorological Satellite Studies, describe that the fire east of Manicouagan Lake in Quebec was centered near 51.6 N and 66.2 W on June 22. Observations from the satellite GOES-13, by comparing the visible channel (0.63 µm) and the IR channel (3.9 µm), showed the development of a very large smoke plume during the day. The footprint of the fire "hot spot", seen in the IR channel, grew in the same time as smoke grew in the visible channel. VIIRS, MODIS and AVHHR showed in the IR shortwave images (3.74 µm) that the size of the footprint of the fire "hot spot" grew rapidly in the period from June 22 at 00:06 UTC to June 23 at 21:09 UTC. The coldest cloud-top IR brightness temperature was -27.5 ° C and seen at 17:09 UTC on June 22, based on a comparison with different channels on VIIRS (0.64 µm visible channel, 11.45 µm IR channel, 3.74 µm

shortwave IR channel and 0.7 μm Day/Night Band). [35]

The smoke was captured east of Newfoundland by MODIS-Aqua on June 23 at 16:05 UTC, written by NASA Earth Observatory. A comparison with CALIPSO measurements at the same location at 16:14 UTC, showed that the smoke plume was on an altitude of 2 to 6 km. The detection was for the smoke plume east of Newfoundland, see Figure 6a. The smoke was high enough to be over the boundary layer, according to the article. [28]. Also seen in the weather analysis at 500mb, see Figure 7, windspeed is 50 knot over the area.

4.3 EVENT 2: SMOKE DETECTION OVER EUROPE

MODIS observations for AOD at 550nm showed that on July 8 one pixel exceeded a value of 2.0, surrounded with values of 0.8 to 2.0, centered over Sweden, see Figure 11. On July 11, one pixel exceeded a value of 1.6, surrounded will values of 0.7 to 1.6, centered on the west coast of Norway over Bergen, see Figure 12. On July 12, one pixel exceeds a value of 1, surrounded with values in the interval 0.5 to 1, see Figure 12.

AERONET observations of AOD for different cites can be seen in table 1. What can be seen, an AOD>1 was detected in France on July 6 and 12, in Sweden on July 8, in Belarus on July 9 and 10 and in Italy on July 13. The detected AOD at Birkenes, Norway, on July 12 corresponds to the same magnitude detected by MODIS, see Figure 12. At Gustav Dalen Tower and Palgrunden, Sweden, on July 8 the AOD values do not reach the magnitude of 2, detected by MODIS, see 11 What should be noted, these cites are located south of the maximum seen by MODIS.

Ceilometer at Oslo-Blindern, Norway, detected the smoke plume on July 8 (Figure 13), 11 (Figure 14a) and 12 (Figure 14b). The smoke plume was on an altitude of 3-4 km and approximately 1 km thick on July 12. LIDAR observation from Cabauw, Netherlands, show the smoke on an altitude at 2 km on July 9, see figure 15 [40]. Ceilometer measurements in Putbus, Germany, detected the smoke plume on the same day, see Figure 16 on July 9, on an altitude of 3 to 6 km [23]. As can be seen in Figure 14b at Oslo-Blindern on July 12 the smoke plume is first seen at 6:00 UTC. Just before 6:00, the AOD increases at Birkenes, see Figure. The Figure also present the fine mode AOD, and this curve follow the total AOD. Therefor, the particles were most likely fine mode particles.

Cite	6	7	8	9	10	11	12	13	14
Norway, B (500nm)	0.4	0.4	0.6	0.2	0.1	0.5	1.1	0.5	0.1
Sweden, GDT (553nm)	0.2	0.5	1.5	0.3		0.2	0.4	0.4	0.7
Sweden, P (555nm)	0.4	0.5	1.3	0.1	0.1	0.2	0.7	0.8	0.3
Belarus, M (440nm)	0.4	0.3	0.2	1.0	1.2	0.5	0.5		0.2
Italy, I (555nm)	0.6	0.5	0.8	0.4	0.4	0.2	0.7	1.1	0.4
France, D (500nm)	1.1	0.6	0.4	0.2	0.1	0.2		0.6	0.9
France, Pa (500nm)	0.3	0.3	0.2	0.2	0.4	0.5	1.0	0.8	0.4

Table 1: AOD by AERONET from July 6 to July 14, 2013, at cites B=Birkenes (58N,8E), P=Palgrunden (58N,13E), GDT=Gustav_Dalen_Tower (58N,17E), M=Minsk (53N,27E), I=Ispra (45N,8E), D=Dunkerque (51N,2E) and Pa=Paris (48N,2E). Values are the highest of the day, hand picked. All Level 2.0 (unscreened and quality assured) except from Birkenes, which is Level 1.5 (unscreened). [24]

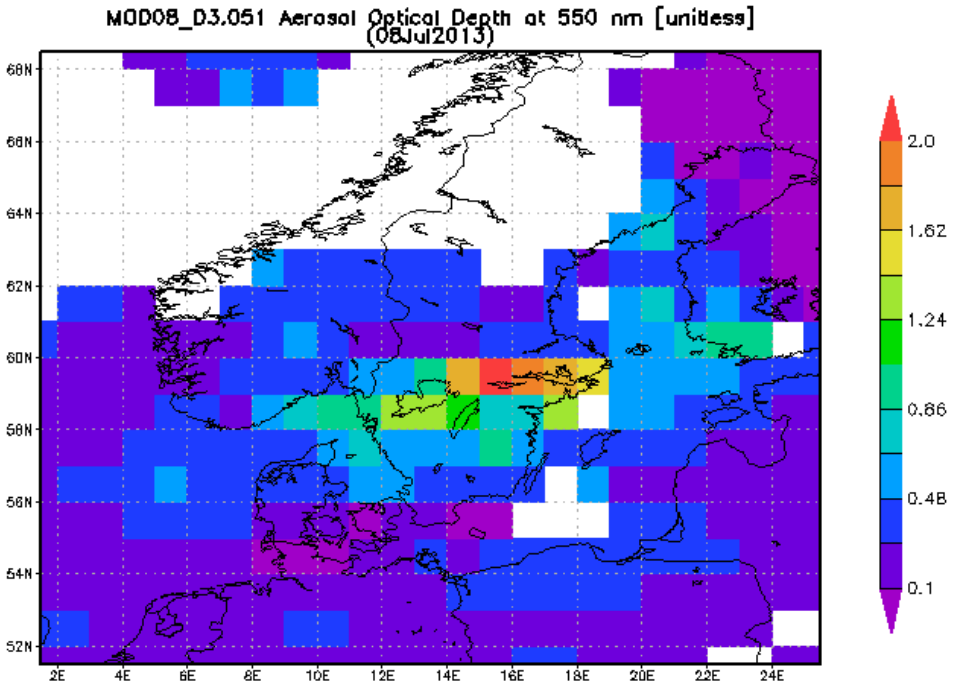

Figure 11: Daily Time-average Lat-Lon Map of Aerosol Optical Depth (AOD) at 550 nm on July 8, 2013, by MODIS-Terra. 1 x 1 degree. Version 5.1. Images downloaded from Giovanni online data system [26].

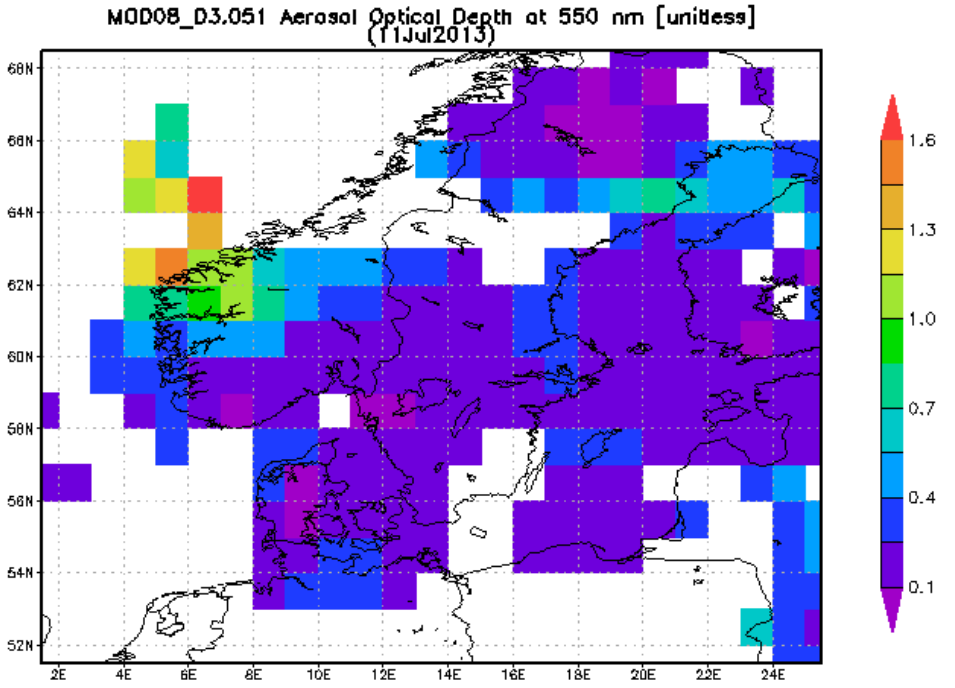

(a)

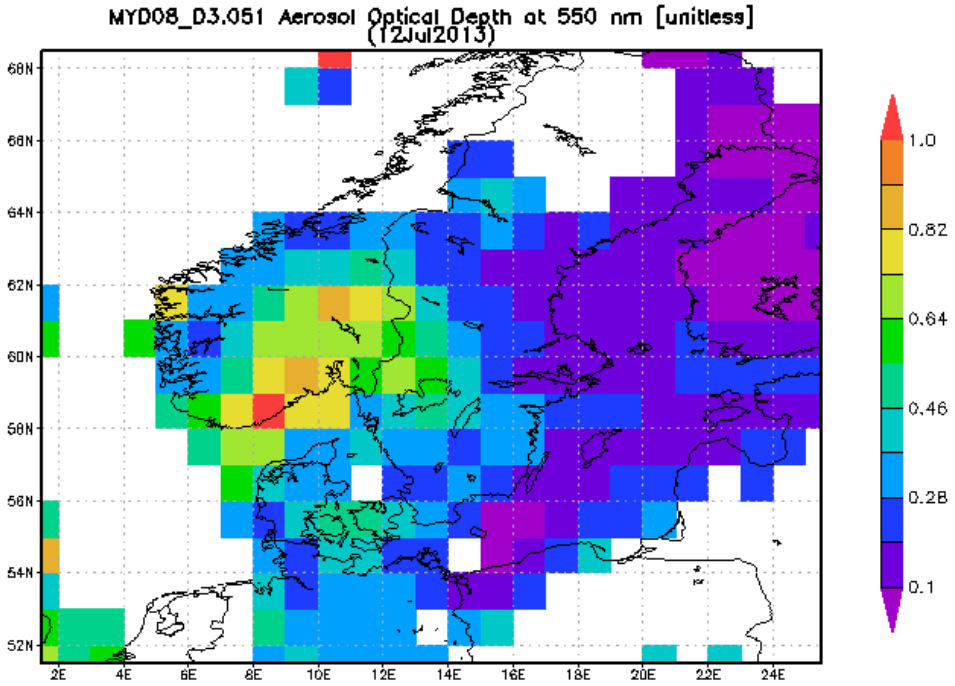

(b)

Figure 12: Daily Time-average Lat-Lon Map of Aerosol Optical Depth (AOD) at 550 nm on July 11 (a), by MODIS-Terra, and July 12 (b), MODIS-Aqua. Both in year 2013. 1 x 1 degree. Version 5.1. Images downloaded from Giovanni online data system [26].

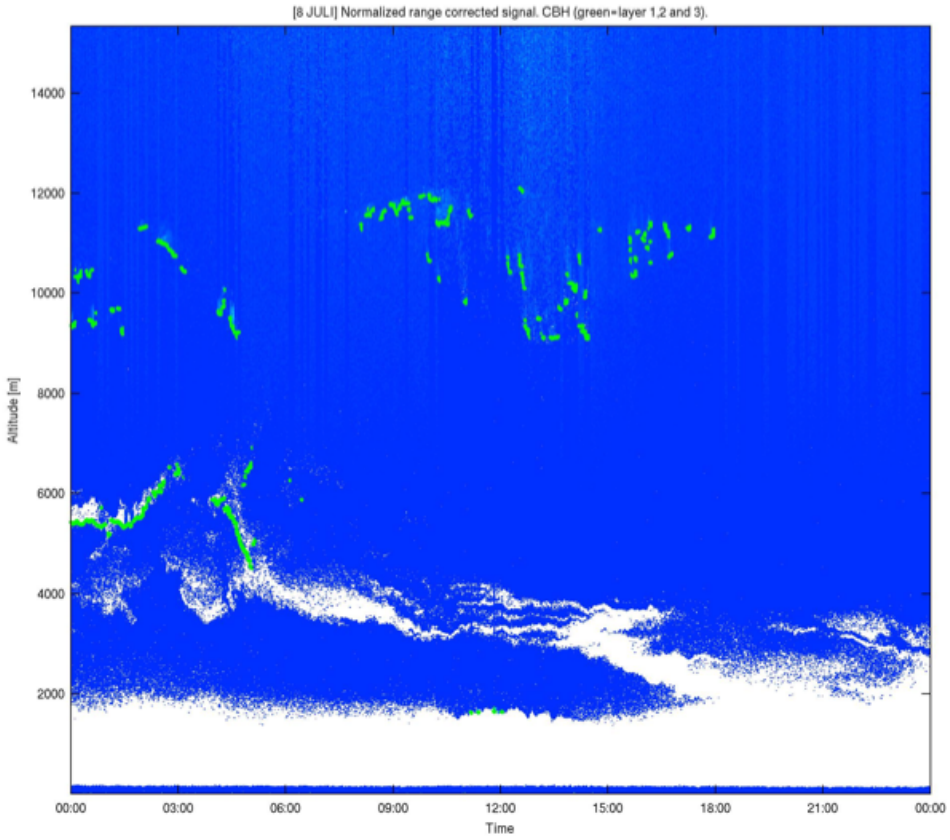

Figure 13: Normalized range corrected signal by Ceilometer at Oslo-Blindern, Norway, on July 8. Green dots represents cloud base height. Time on the X axis and altitude in kilometer on the Y-axis.

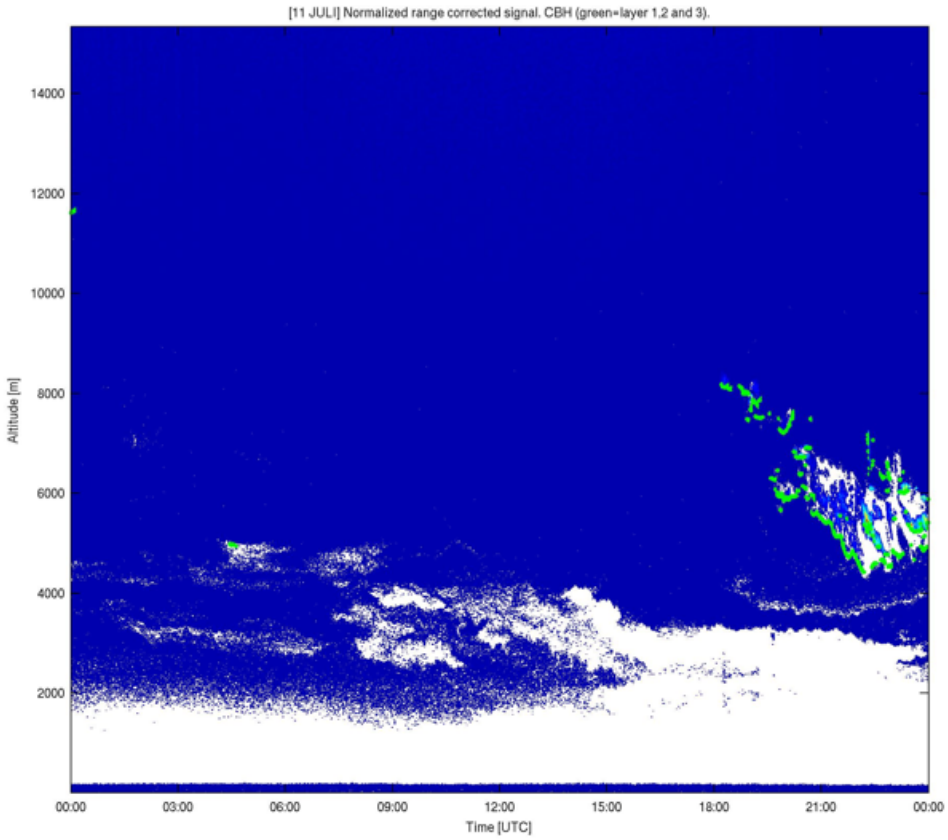

(a)

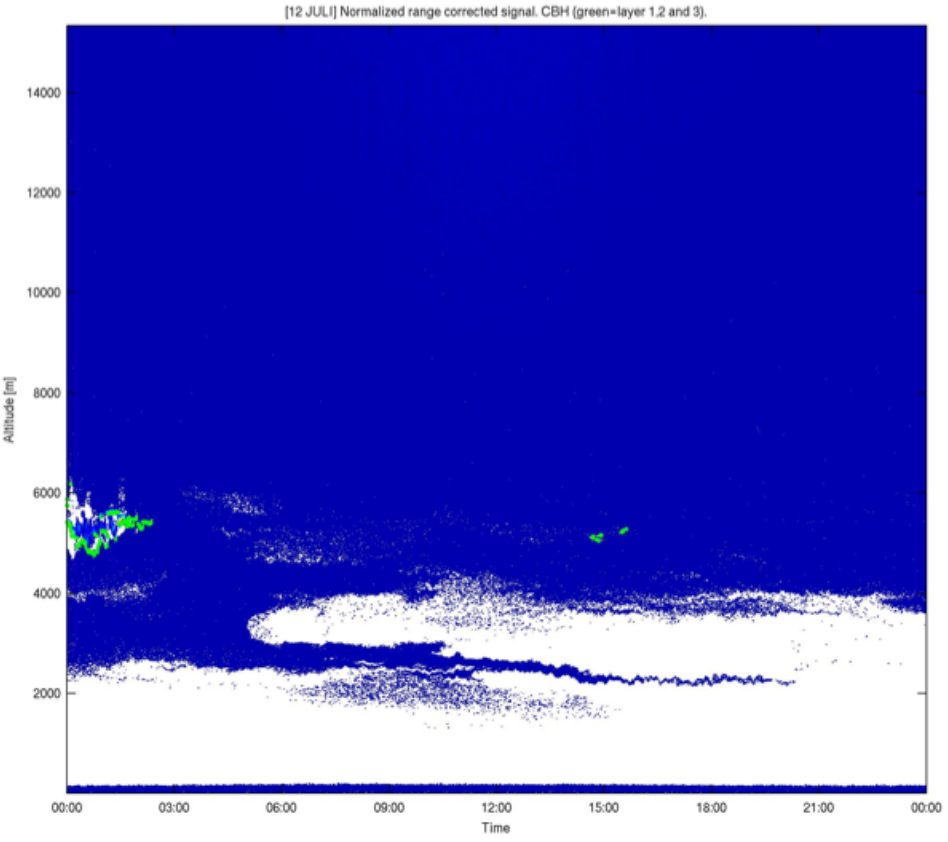

(b)

Figure 14: Normalized range corrected signal by Ceilometer at Oslo-Blindern, Norway, on July 11 (a) and July 12 (b), 2013. Green dots represents cloud base height. Time on the X axis and altitude in kilometer on the Y-axis.

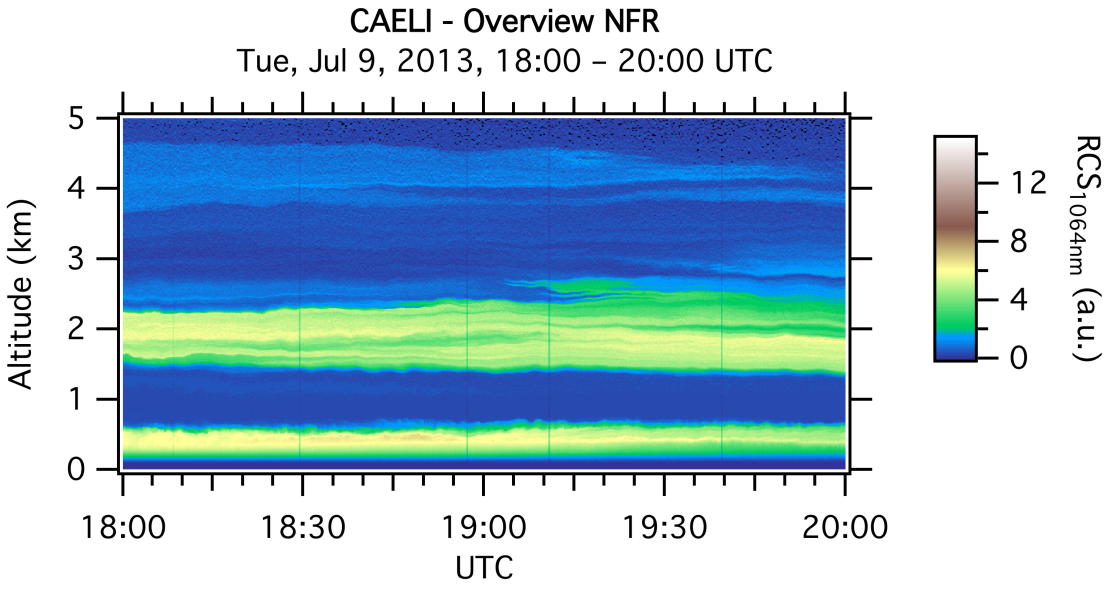

Figure 15: LIDAR observation from Cabauw in Netherlands on July 9, 2013, provided by the Royal Meteorological Institute of Belgium [40].

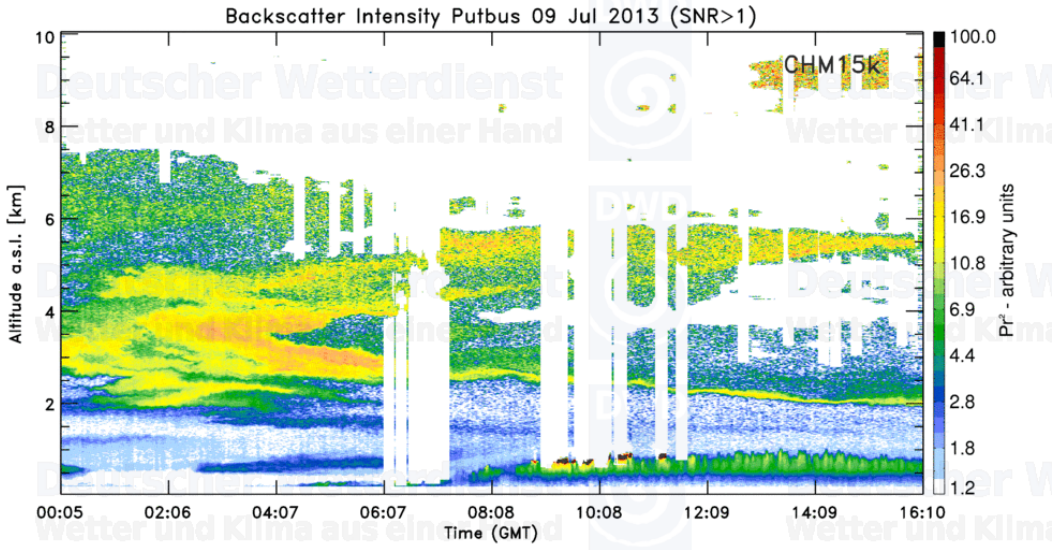

Figure 16: Ceilometer (CHM 15k) measurements in Putbus, Germany, on July 9, 2013. [23]

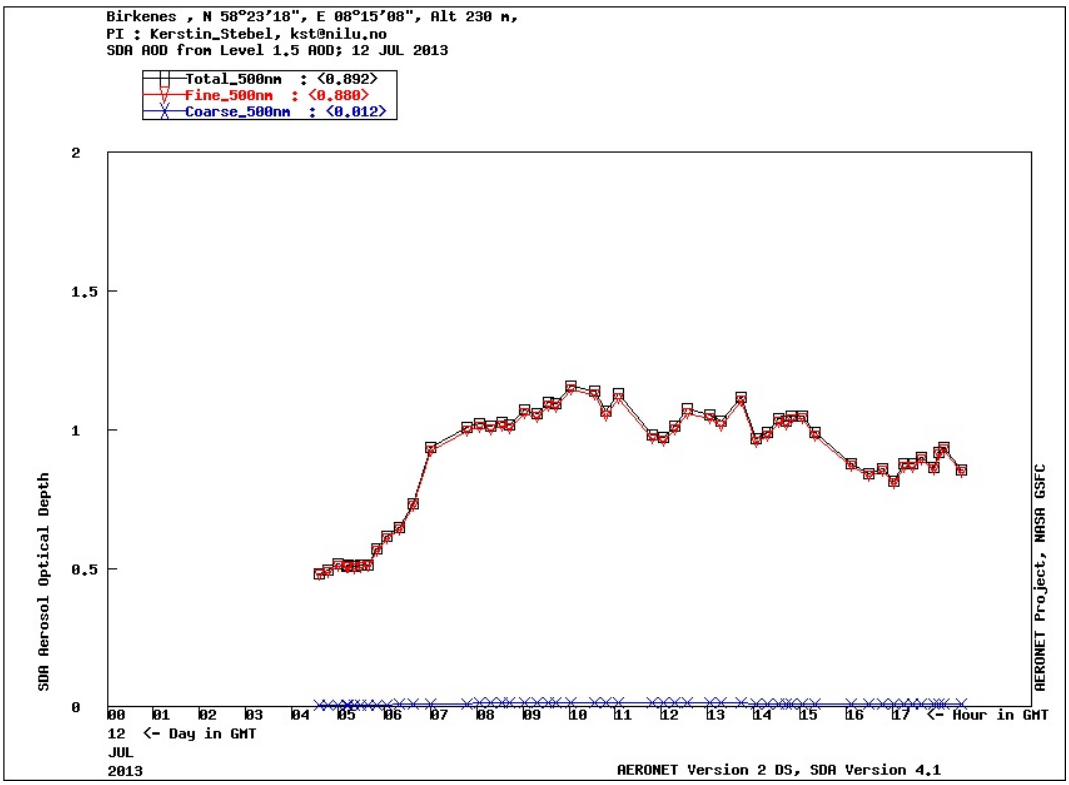

Figure 17: Spectral De-Convolution Algorithm (SDA) Retrievals of the Aerosol Optical depth at 500nm on July 12, at Birkenes, Norway. Total, fine mode and coarse AOD represents the black, red and blue curves, respectively. [26]

4.4 EVENT 2: WILDFIRE RESEARCH

Detections by OMPS, see Figure 18 from July 4 to 6 and Figure 19 from July 7 to 9, show high concentrations over the Atlantic. By the day of July 6, the smoke plume leaves the coast of Canada, outside Newfoundland. By the day of July 8, high AI values are seen over Sweden. The smoke plume has the same position and structure as the high AOD, detected by MODIS, see Figure 11.

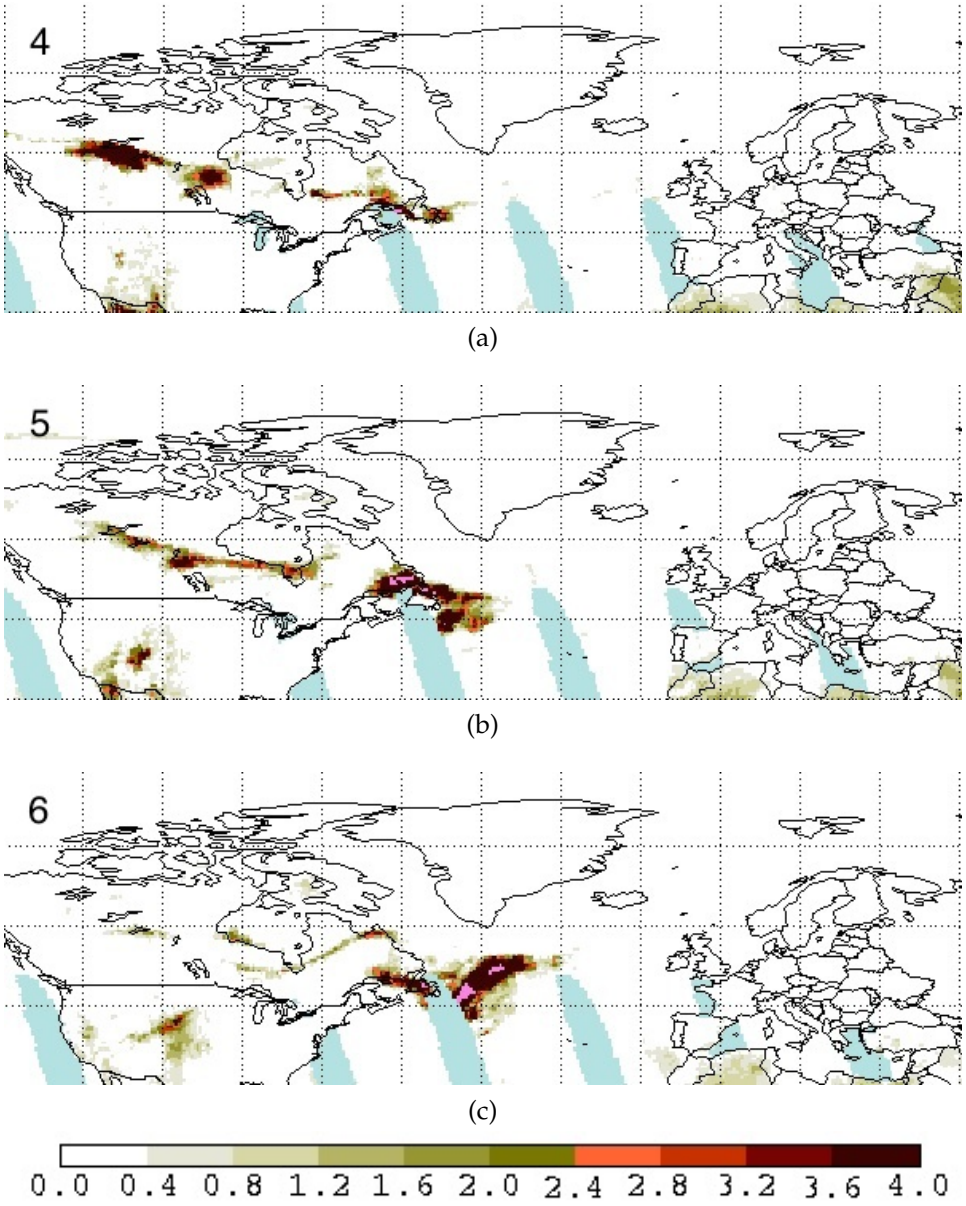

Figure 18: OMPS Aerosol Index (AI) Maps on July 4 (a), July 5 (b) and July 6 (c), from the satellite Suomi-NPP. All from year 2013. [31]

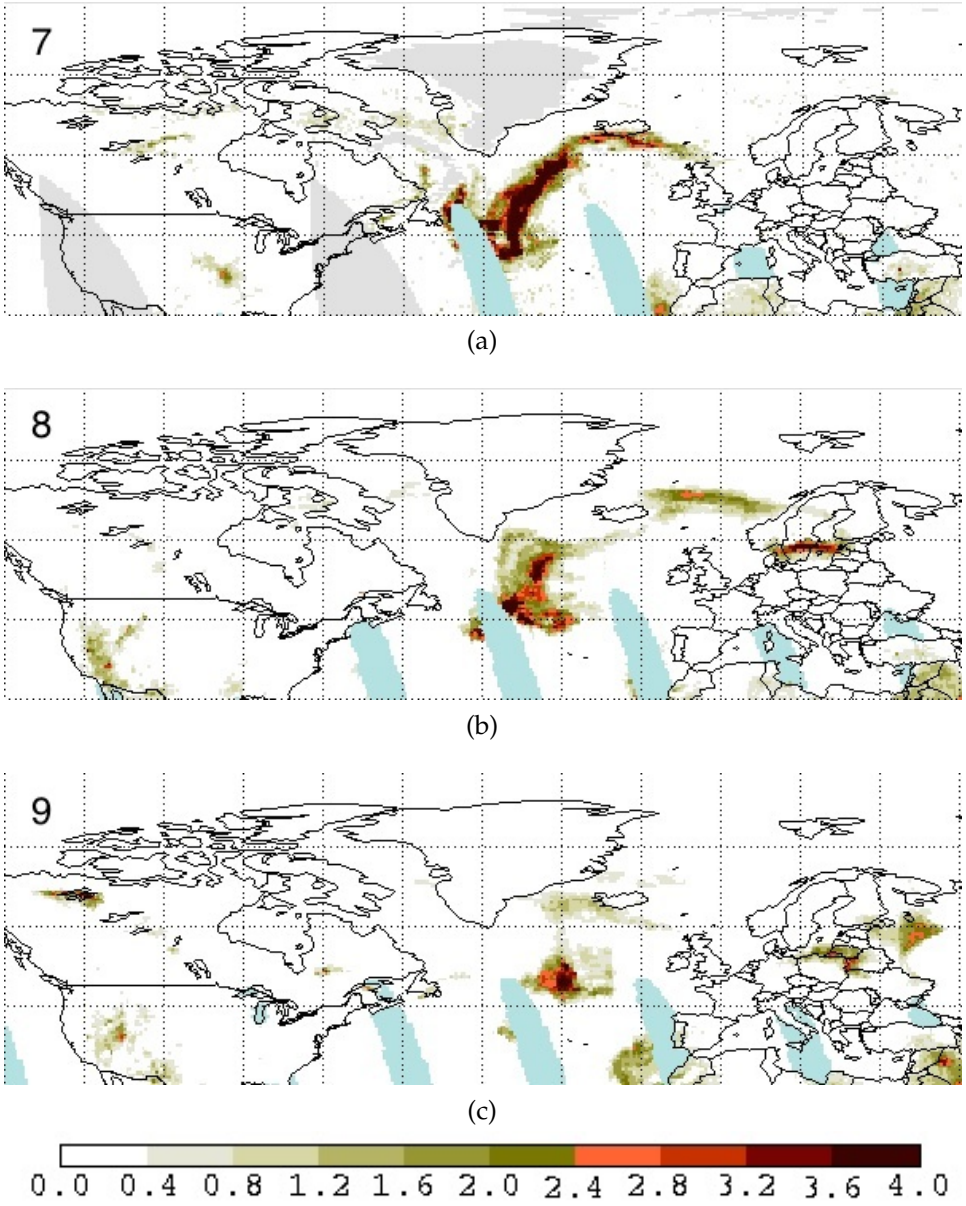

Figure 19: OMPS Aerosol Index (AI) Maps on July 7 (a), July 8 (b) and July 9 (c), from the satellite Suomi-NPP. All from year 2013. [31]

Monotoring atmospheric composition and climate, macc, made a MACC-II's global forecasting of the period, which showed the smoke originated back to wildfires in Canada, see Figure 20 The forecast was supported with observations from MODIS, MOPITT (Measurements Of Pollution In The Troposphere) and IASI (Infrared Atmospheric Sounding Interferometer) instruments. The model is initiated with values from GFAS algorithm, which is a daily global map for the emissions of the observed fires in Canada and United States. Validation of the 5-day forecast was done with aircraft observations, measuring carbon monoxide concentration. The carbon monoxide

concentration was detected on an altitude of 3 km at Frankfurt airport and 2 km at Paris airport on July 6, see Figure 21. [23]

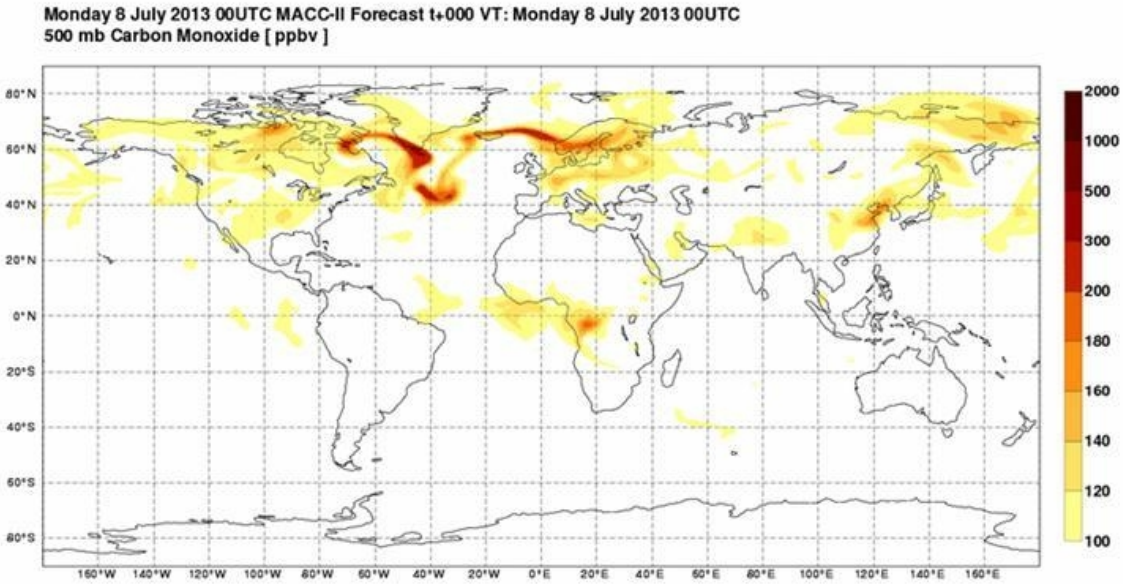

Figure 20: Carbon monoxide at 500mb on July 8 00 UTC, 2013 [23].

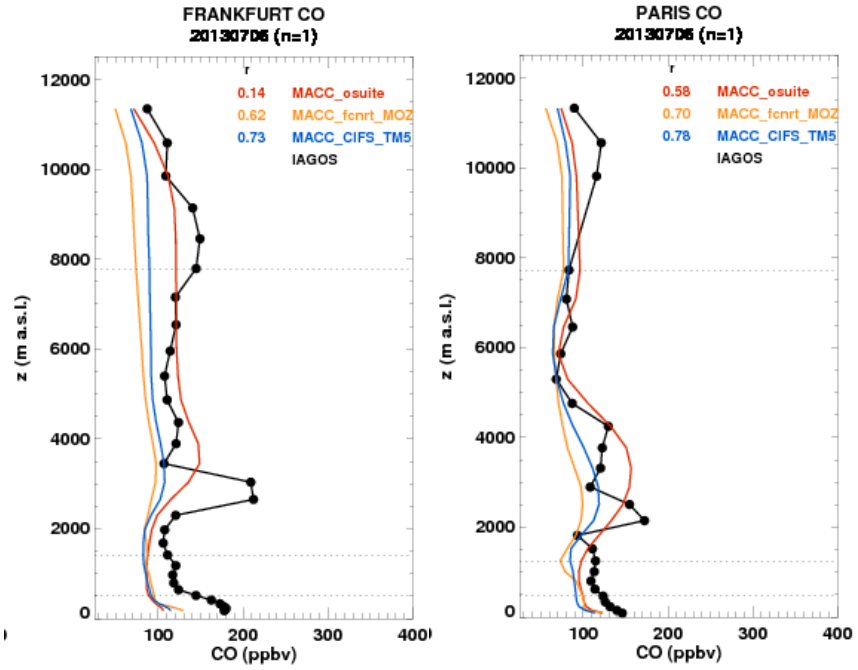

(a) (b)

Figure 21: MACC-II forecasts of CO profiles compared to IAGOS aircraft observations over Frankfurt and Paris on July 6 [23].

Geopotential height at 500mb on July 4, see Figure 22a, show a low pressure northeast of James Bay with winds of 55 knot over Newfoundland and Labrador. Geopotential height on July 7 show a trough over the Atlantic. By looking at AI on July 7, see figure 19a, the isohyps and the smoke plume has the same structure in the trough over the Atlantic. A back trajectory by the HYSPLIT model further again indicates that the smoke originated from Quebec, see Figure 23. The trajectory also goes over the Eastmain region east of James Bay.

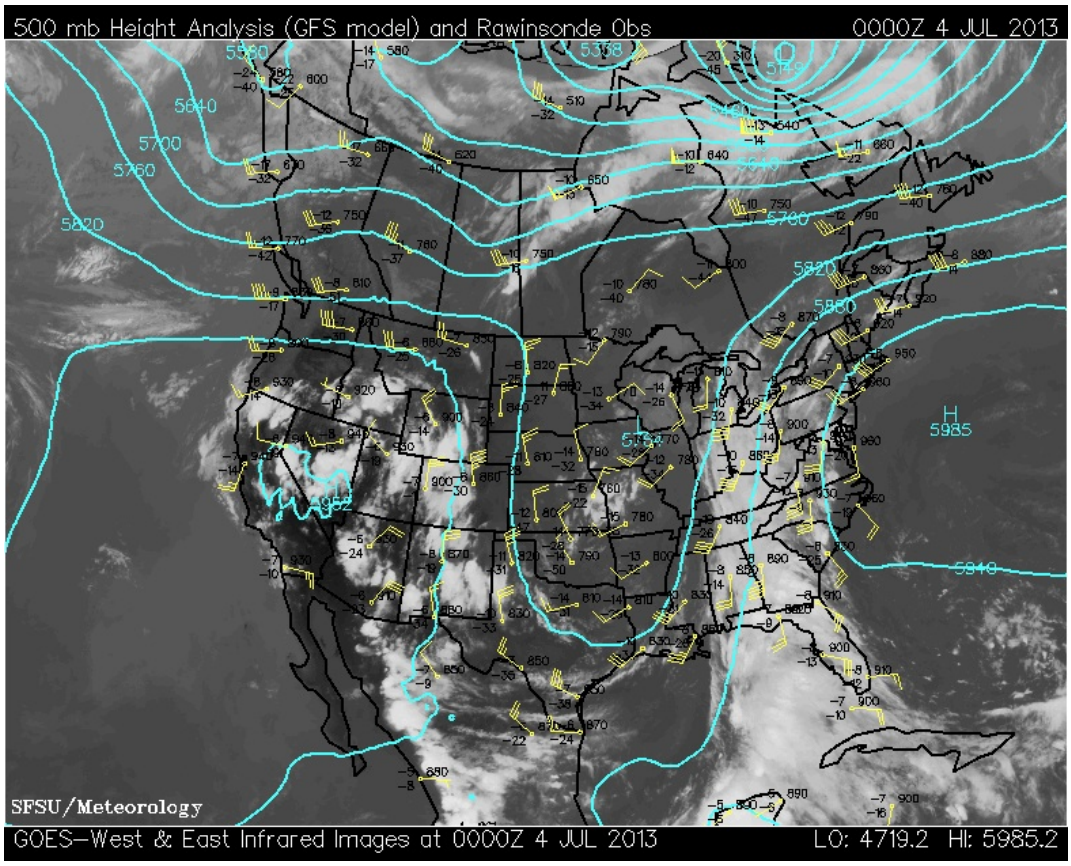

(a)

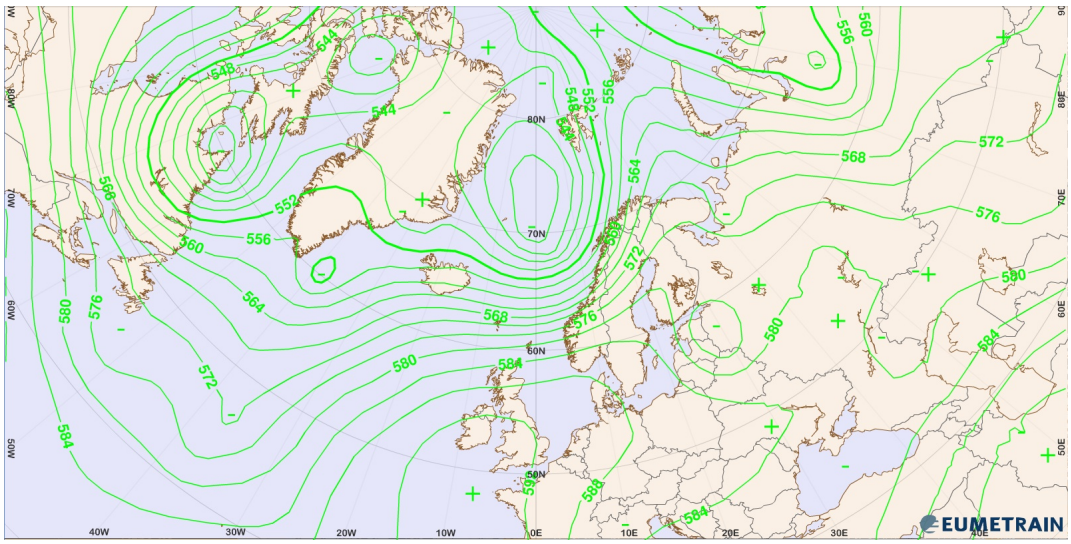

(b)

Figure 22: Geopotential height at 500 mb on July 4 at 12:00 UTC (a), by California Regional Weather server [4], and July 7 at 12:00 UTC (b), by Eumettrain [14]. All in year 2013. Figure (b) is expressed in geopotential decameters (gpm.).

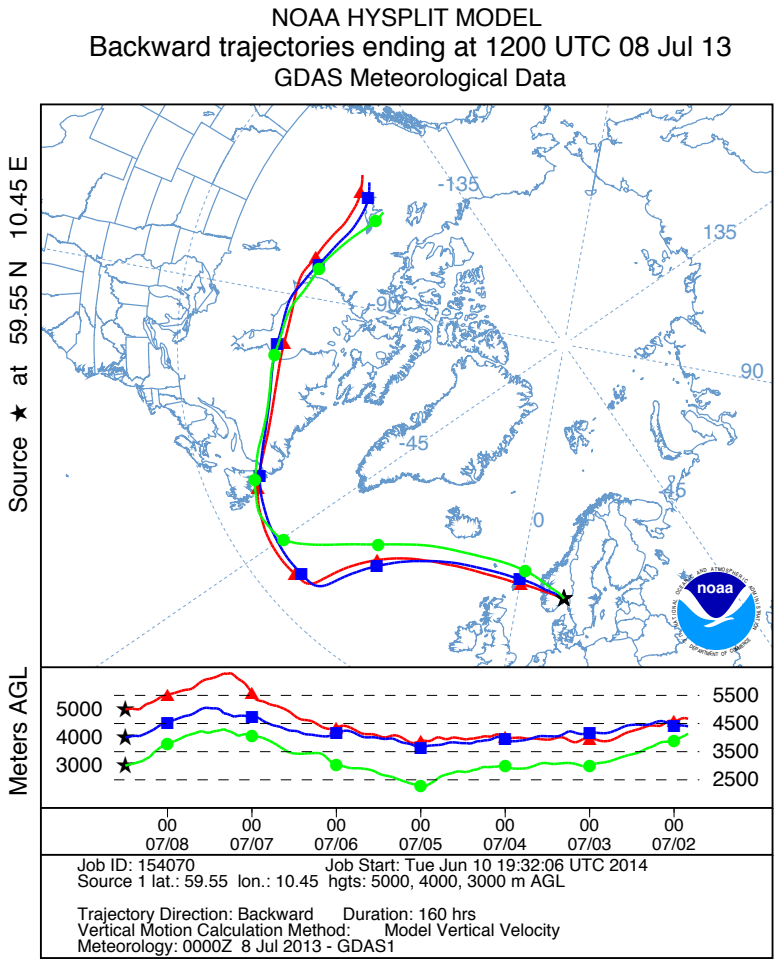

Figure 23: NOAA HYSPLIT model. Back trajectories from Oslo, Norway, starting on July 8 at 12 UTC, 2013. Starting altitudes are: 3000 km (red), 4000 km (blue) and 5000 km (green). [12]

Canadian Wildland Fire Information System reported on July 10 an weekly area burned of approximately 850 000 ha, which was four times the 10-year average. Quebec accounted for 66% of the area burned. [7]

PyroCb, by Cooperative Institute for Meteorological Satellite Studies, de-

scribed that fires in the Eastmain region of Quebec on July 4 produced a large amount of smoke, detected in the visible channel 0.63µm by GOES-13. After 21:55 UTC, several dense smoke plumes and pyrocumulonimbus were observed. The "hot spots" in increased during the day, seen by short-wave IR images (3.9 µm) by GOES-13. The IR brightness temperatures was observed to around -40 °C, by longwave IR image from GOES-13. [36]
The Eastmain fire ignited by lightening on May 25. The fire was the 2nd largest fire since records began 1959. On July 4 the smoke cut the power to Montreal's subway system and to 10% of the population of Quebec. [6] According to CBC News 261 people had to be evacuated by plane from the Cree community of Eastmain on June 28 [8].

4.5 VALUES TO INSERT IN WRF

The area of interest in this thesis is the southern part of Norway. According to MODIS observations, the area got mostly influenced by the smoke on July 11 and July 12, see Figure 12. AOD detection by MODIS and AERONET pointing towards an value of at least 1.1. Simulations in this thesis will therefor investigate the surface temperature effect of an AOD=1.1 from July 11 to 12, 2013. The model will be run for two extra days to investigate what is happening to the domain. The domain will be a size of the detected AOD values on July 12, by MODIS. The AOD value will be placed on an altitude of 3-4 km, because of the detection by ceilometer, see Figure 14.

5 METHOD

Research about wildfires and detection of smoke over Europe were researched in chapter 4. Based on this information, see section 4.5, the WRF-model was used to simulate the influence of the smoke on the surface temperature. This chapter will describe the method applied by WRF, see section 5.1. The chapter will also contain a description of the synoptic observations from Eklima and ERA-Interim, since these are going to be compared with the simulations, see section 5.2 for Eklima and section 5.3 for ERA-Interim.

5.1 WRF

The **W**eather **R**esearch and **F**orecasting (WRF) model is a numerical weather prediction system. WRF has a Pre-Processing System called WPS, which puts geological and meteorological fields into initialization data. It has two dynamical solvers, one for research and one for operational forecasting, named ARW (Advanced Research WRF) and NMM (Nonhydrostatic Mesoscale Model), respectively. [42, Skamarock et al. (2008)]
In this study, version WRFV3.5.1 is used in combination with the dynamical solver ARW.
AOD, single-scattering albedo and asymmetry parameter controls the direct radiative effect of aerosols, see chapter 2 under section 2.1. AOD is currently set to zero in WRF and single-scattering albedo and asymmetry parameter has set values, see section 5.1.5 below for exact values. AOD can therefor be changed in the domain. One simulation with an selected AOD and one with zero AOD can give us knowledge about the affect of the surface temperature with and without aerosols.
A global model need to provide boundary conditions for the domain. Therefor, the domain need to be large enough to get unaffected by these boundary conditions. But, as the purpose in this study is to change AOD to observed values for the whole domain, the size is too large to correspond to AOD observations by MODIS. To solve this problem, the method of an One-way Nested Run using Ndown for a parent and nested domain was chosen. Not only will it solve that problem, the method will also give less computation costs.

5.1.1 *Model setup*

Two domains are selected, one parent domain with horizontal grid points 140 x 140 and one nested domain with 40 x 40. The nested domain i located over southern Norway. Both domains have the same resolution of 15 x 15 km.

5.1.2 *Running the WPS*

For real-data cases, as the case in this study, WPS need to be used to obtain files to put into the initialization program *real.exe*. WPS is therefor a preparation process, which includes three independent programs:

1, *geogrid.exe*: Define the size and location of the domains and interpolate static geographical data to the grid points, see section 5.1.1 for sizes. Lambert projection is used, as it is in general most suited for mid-latitude domains.

2, *ungrib.exe*: Extract meteorological fields from real time data set. Meteorological fields is from ERA-Interim every sixth hour for the period July 11-14 (2013), start time 00 UTC and end 18 UTC, provided by Bjørg Rognerud (University of Oslo, METOS). Description of ERA-Interim can be seen in section 5.3. For *ungrib.exe* to access certain meteorological data, a specific Vtable need to be used. In this case Vtable is for ECMWF data, provided by Kjetil Schanke Aas (University of Oslo, METOS).

3, *metgrid.exe*: Horizontally interpolate meteorological fields to the model domain.

A successful completion of WPS give NetCDF-files every sixth hour to be used in the initialization program.

5.1.3 *Running WRF*

WRF contains four different programs. Used in this study is the initialization program for real-data cases (*real.exe*), the numerical integration program (*wrf.exe*) and the one-way nested program (*ndown.exe*). The last program is to do tropical storm bogussing (*tc.exe*) and is not used. The program *real.exe* uses input data from WPS, see previous section 5.1.2. A successful completion creates input and boundaries for parent and nested domain to be run by *wrf.exe*. The program *ndown.exe* is run in-between the two simulations. The initial and lateral boundary conditions from the parent domain will than be obtained in the run for the nested domain.

5.1.4 *One-way Nested Run using Ndown*

The general purpose of a One-way Nested Run using Ndown is to make a finer-grid-resolution run of the nested domain and use the initial and lateral boundary conditions from the coarser domain (parent domain). In this study the only purpose was to be able to use the initial and lateral boundary conditions from the parent domain so a smaller domain could be used with an selected AOD. The nested domain is therefor not a finer-grid-resolution and has the same resolution as the parent domain.
In figure 24, the process of doing a One-way Nested Run using Ndown is illustrated. Running *real.exe* gives wrf input (wrfinput) and wrf boundaries (wrfbdy) for the parent and nested domain. First *wrf.exe* is run for the parent domain. The output file (wrfout) and the wrf input file from the nested domain (wrfindi) is then run by *ndown.exe*. *ndown.exe* creates wrf input and boundaries to be run again by *wrf.exe*, which is the simulations for the nested domain. The nested domain is so on based on boundaries for the parent domain.

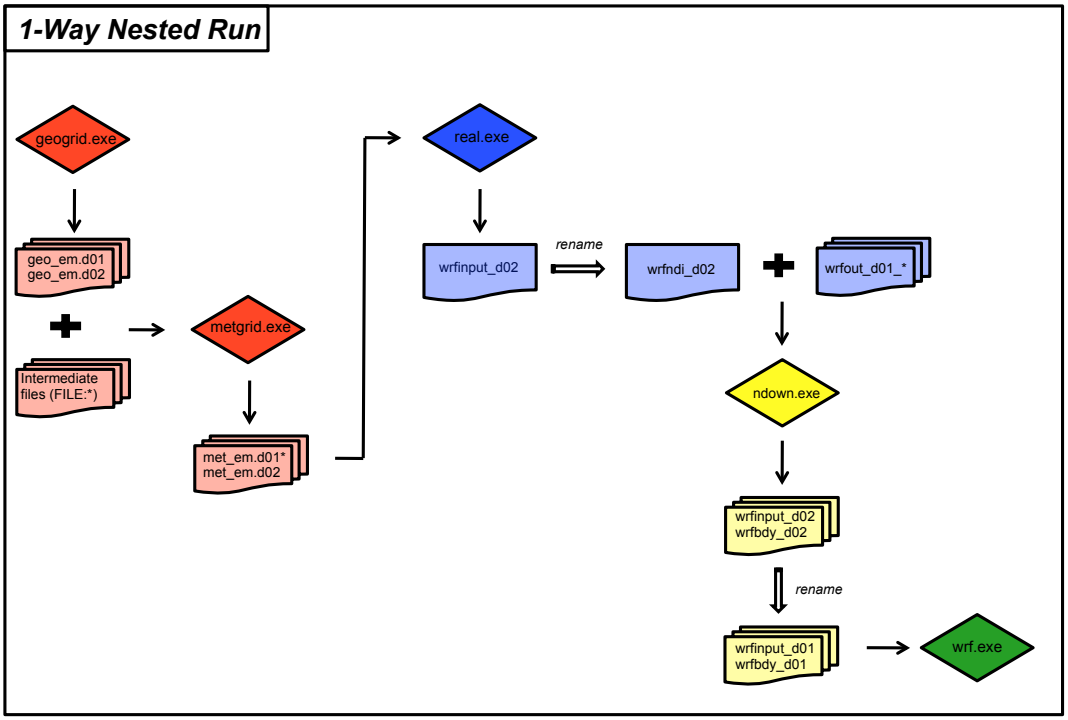

Figure 24: One-Way Nested Run Using Ndown [47].

5.1.5 *Physics and change of AOD for nested domain*

The schemes used for the different parameterizations are: WRF Single-Moment 3-class scheme (Microphysics), CAM scheme (Longwave Radiation), CAM scheme (Shortwave Radiation), Eta similarity (Surface layer), Noah Land

Surface Model (Land surface), Mellor-Yamada-Janjic scheme (Planetary Boundary layer) and Betts-Miller-Janjic scheme (Cumulus Parameterization). The mainly focus in this study is the CAM Shortwave scheme. The scheme is based on the principle of δ-Eddington, see chapter 2 under section 2.7. Spectral band number 8 is defined as the visible band, from 0.35 to 0.64 μm. For every grid box, vertical level and spectral band, the total aerosol optical depth is computed, currently set to zero in default mode. The total aerosol optical depth is the sum of different aerosol groups. One AOD group is called background aerosol depth and has a single-scattering albedo of 0.99, asymmetry parameter of 0.74 and a forward scattered fraction of 0.55. The method applied is setting a selected AOD for spectral band number 8 on three vertical levels for all grid boxes in the domain. Selected levels are chosen to correspond to the altitude of aerosol layer on an altitude of 3-4 km, see chapter 4 under section 5.1.

5.1.6 *Calculation of CLWP*

One of the output parameters chosen to be investigated is the cloud liquid water path (CLWP). Here the calculations of the CLWP is presented.
Using ideal gas law, the pressure for dry air, p_d, and water vapor, e, is given by

$$p_d = \rho_d R_d T \qquad e = \rho_v R_v T \tag{24}$$

where ρ_d and ρ_v is the density for dry air and water vapor [kg m^{-3}], respectively, gas constants R_d =287.0 $JK^{-1}kg^{-1}$ and R_v =461.5 $JK^{-1}kg^{-1}$ for dry air and water vapor, respectively, and T is the temperature [K]. The total pressure is then

$$p = p_d + e = T(\rho_d R_d + \rho_v R_v) \tag{25}$$

The water vapor mixing ratio is defined

$$Q_v = \frac{m_v}{m_d} \tag{26}$$

where m_v and m_d is the mass of dry air and water vapor [kg]. The density of water vapor is given by

$$\rho_v = \frac{m_v}{V} \tag{27}$$

where V is the volume [m^3]. With equation 26 and 27 in equation 25, the pressure is

$$p = T\rho_d(R_d + R_v Q_v) \tag{28}$$

and the density of dry air can be written

$$\rho_d = \frac{p}{T(R_d + R_v Q_v)} \tag{29}$$

The potential temperature is defined

$$\theta = T(p_0/p)^{R/C_p} \tag{30}$$

where the reference pressure i p_0=1000hPa and R is assumed to be R_d and C_p assumed to be for dry air C_{pd}=1004 $JK^{-1}kg^{-1}$. The geopotential is defined

$$\phi = gZ \tag{31}$$

where g=9.81 [m $s^{-}2$] is the gravitational constant and Z is the geopotential height [m]. The CLWP is given by

$$CLWP = \int_{Z_0}^{Z} Q_c \rho_d dZ \tag{32}$$

where Q_c is the cloud mixing ratio defined as m_c/m_d where m_c is the mass of cloud water. Combining equation 29, 30 and 31 the CLWP is given

$$CLWP = \frac{p(p_0/p)^{R/C_p}}{\theta(R_d + R_v Q_v)} Q_c dZ \tag{33}$$

5.2 EKLIMA

Eklima is a web-based portal by the Norwegian Meteorological Institute, which provide observation data from weather stations in Norway. The mainly purpose of the obtained observations is to compare the temperature with the 2 meter temperature simulated by WRF. Stations are selected according to cloud free grid points in WRF, which will further be discussed in the chapter of result 6 under section 6.2. Data for air temperature is available four times a day; 00, 06, 12, and 18 UTC. [33]

5.3 ERA-INTERIM

ERA-Interim, provided by ECMWF, is a numerical description of the atmosphere in recent history, so-called reanalysis. Reanalysis is created by combining models and observations. Data assimilation is done with 4-dimensional

variational analysis (4D-Var) with a 12 hour analysis window. ERA-Interim is a global data set from 1979 to present. The grid point resolution is a reduced Gaussian N128 with a latitude/longitude resolution of 0.75 x 0.75°. Parameter used in this study, is the analysis of the "2 meter temperature". Analysis is a combination of short-range forecast data and observations. The "2 meter temperature" is analyzed every sixth hour, which also is the selected time step of the provided data. [13]

6 RESULT AND DISCUSSION

Simulations by WRF have been tested with different values of AOD. The main idea was to compare two simulations, one with zero AOD and one with the observed value of 1.1. Other simulations are: AOD=10 and AOD=100. The simulation time was from July 11 to 14, 2013, where the days in this study will be called Day 1, 2, 3 and 4, respectively. Parameters investigated are the surface temperature (2 meter temperature), downward shortwave (SW) flux and the cloud liquid water path (CLWP). The selected parameters are based on the high dependence of downward SW-flux on the surface temperature. The downward SW-flux is further on highly dependent on the presence of clouds.

As we know, a model is far from perfect. It can not simulate the true state of the atmosphere. As close as we can come the true state, are observations. It is therefor necessary and interesting to compare these model results with observations.

In section 6.1, the difference of each parameter for an AOD=1.1 and an AOD=0 will be presented and discussed as a view over the whole domain at one time for each day. In section 6.2, the surface temperature, downward SW-flux and CLWP will be presented as a time series of 10 averaged grid points. Three time series will be presented. One time series will contain the simulated surface temperature for an AOD=0, AOD=1.1, AOD=10 and AOD=100 as well as synoptic observations from Eklima and analysis from ERA-Interim. The other two time series, will show the difference of every AOD$\neq$0 with an AOD=0 for the surface temperature and downward SW-flux, respectively. They will also include the difference of CLWP for an AOD=1.1 and AOD=0.

6.1 DAILY DOMAIN COMPARISON

Simulation difference between AOD=0 and AOD=1.1 over the whole domain is presented in Figure 25 (Day 1 and 2) and Figure 27 (Day 3 and 4) for parameters: surface temperature (top figures), downward SW-flux (middle figures) and CLWP (bottom figures). CLWP for the simulation with an AOD=0 are presented in Figure 26 (Day 1 and 2) and in Figure 28 (Day 3 and 4).

Over all, the surface temperature difference is clearly negative dominated for all days. This means, by a simulation of an AOD=1.1 the surface temperature gets lower in most grid points compared with a simulation of an AOD=0. Simulations also show that most of the grid points for an AOD=1.1 receives less downward SW-flux. The CLWP for AOD=0 show that on Day 1 and 2 there is almost clear conditions, see Figure 26, and after two days clouds are almost covering the whole domain, see Figure 28.

The cooling effect is only seen over land and not over the ocean and the biggest lake in Sweden, Vänern. The surface temperature difference over the ocean is mostly zero. As the model has constant ocean temperature, the air temperature will be close to that temperature and no difference will be seen. The ocean temperature also effect the coast of Norway, where values than become close to zero.

In some grid points over land, the temperature difference is positive or largely negative. Positive values means that in some grid points the surface temperature is higher for the simulation by an AOD=1.1, compared with an AOD=0. Largely negative values means that the temperature is largely lower in the AOD=1.1 run. For instance, the temperature difference is seen to be -1.4, see Figure 25a, and +1.5, see Figure 25b. The positive and largely negative values are connected to a larger downward SW-flux difference. The downward SW-flux difference is connected to the CLWP difference. In other words, the temperature is largely dependent on the presence of clouds for each simulation.

In some cases the temperature difference is positive without the presence of clouds. This is for example seen in the bay of Oslo and over the lake Vänern on Day 2, see Figure 25b. The effect is not seen for the same extent on Day 3 and Day 4. But as can be seen, these are days with clouds in the area, see Figure 28a and 28b. As the run with an AOD=0 has a warmer surface, more convection should be created and the process of sea breeze can be larger. Higher winds over the ocean can decrease the air temperature and the difference will be positive.

CLWP becomes different for the two simulations. Due to more convection in the run by AOD=0, values of CLWP difference are larger for positive values. Clouds are highly sensitive in numerical weather models. The atmospheric state is highly dependent on the initial state. After time, two almost alike initial state will diverge from each other. Even though the simulations has the same physics, a slightly change will contribute to different conditions.

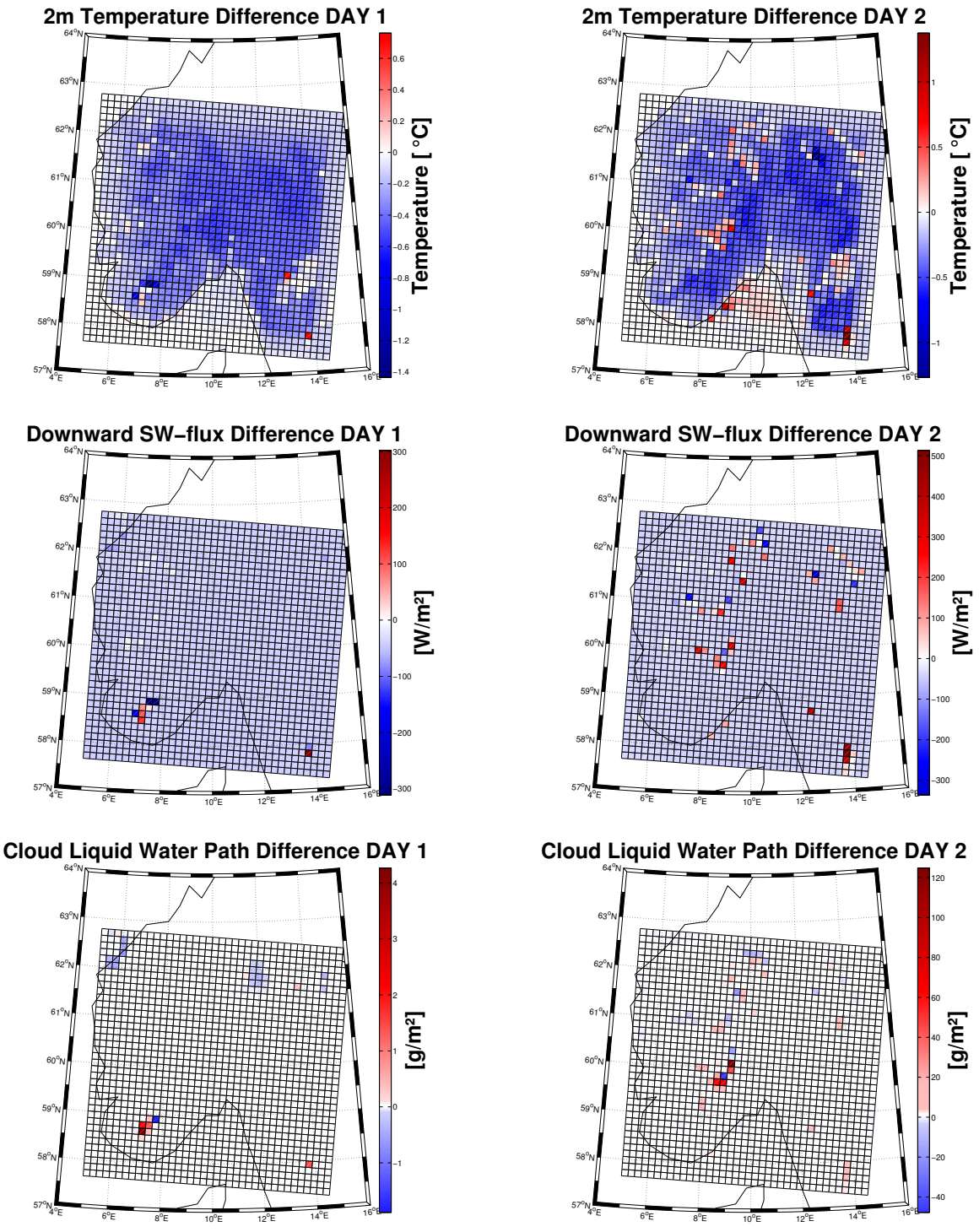

(e) (f)

Figure 25: Difference between WRF simulations of an AOD=0 and AOD=1.1 for surface temperature (Day 1 (a) and Day 2 (b)), downward SW-flux (Day 1 (c) and Day 2 (d)) and cloud liquid water path, CLWP (Day 1 (e) and Day 2 (f)). All plots are at 14:00 UTC.

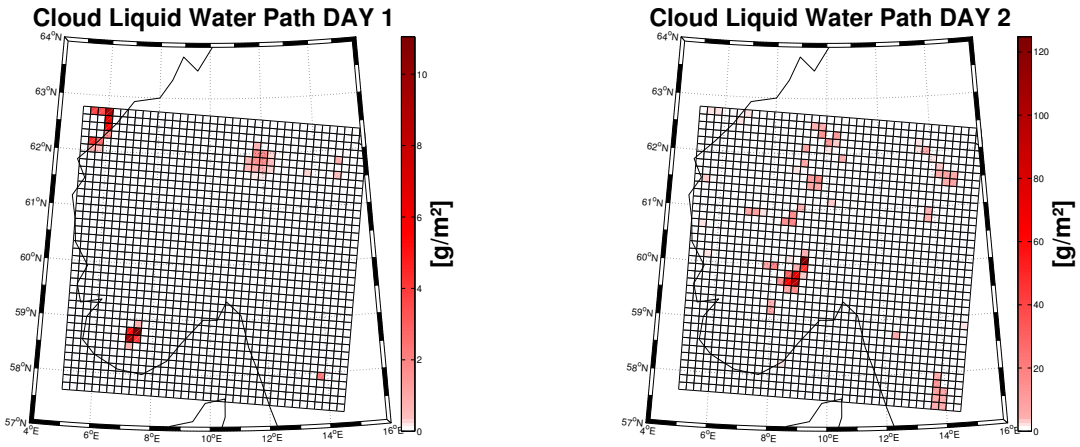

(a) (b)

Figure 26: Cloud Liquied Water Path (CLWP) for simulation AOD=0 on Day 1 (a) and Day 2 (b). All plots are at 14:00 UTC.

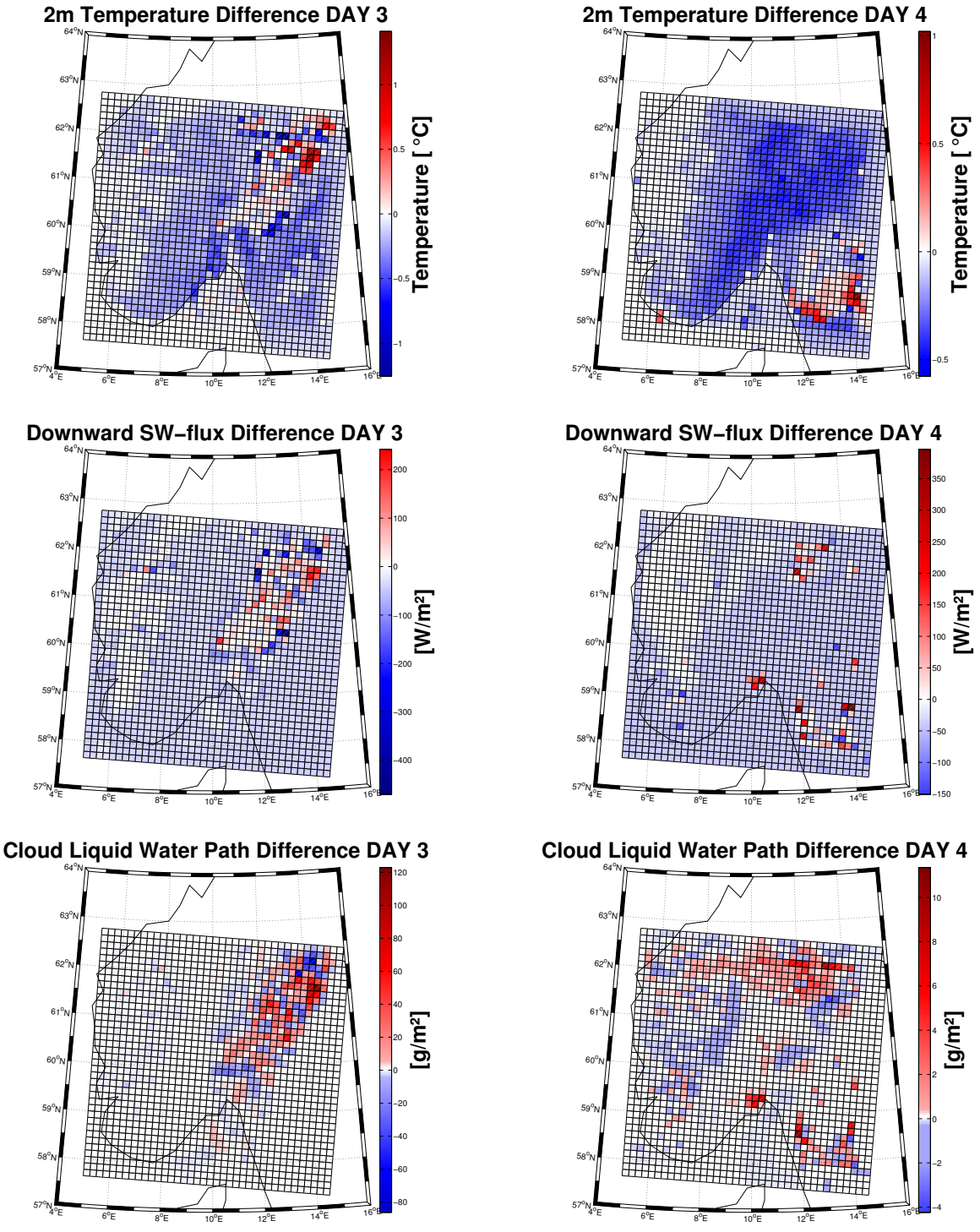

(e) (f)

Figure 27: Difference between WRF simulations of an AOD=0 and AOD=1.1 for surface temperature (Day 3 (a) and Day 4 (b)), downward SW-flux (Day 3 (c) and Day 4 (d)) and cloud liquid water path CLWP, (Day 3 (e) and Day 4 (f)). All plots are at 14:00 UTC.

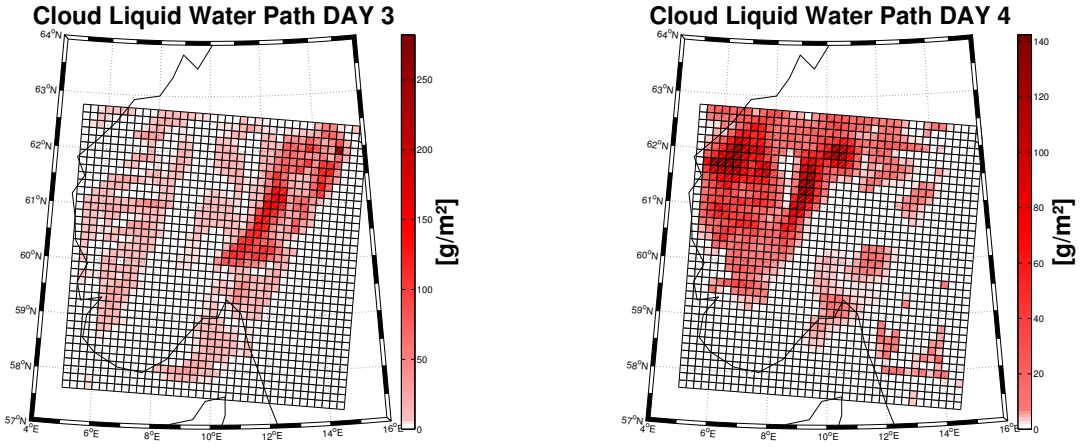

(a) (b)

Figure 28: Cloud Liquied Water Path (CLWP) for simulation AOD=0 on Day 3 (a) and Day 4 (b). All plots are at 14:00 UTC.

6.2 TIME SERIES AND OBSERVATIONS COMPARISON

Section 6.1 showed a cooling effect over land with an AOD of 1.1. To further research the exact value of the cooling effect, the surface temperature is chosen to be average over 10 grid points and be presented as a time. The 10 grid points are distributed over the inland in Norway, since the temperature at the coast is obviously influenced by the ocean, see previous section 6.1. As a comparison with synoptic observations is desired, the grid points are chosen to be closest to a synoptic station with available data of the surface temperature. As discussed in section 6.1, clouds play a big role for the temperature difference and downward SW-flux difference. The temperature difference can be largely positive or largely negative in the presence of clouds. In those cases the values will not correspond to a realistic value of the temperature difference with and without aerosols. The 10 average grid points are therefor consciously selected to not consist of CLWP. As the cloud cover is dominating for Day 3 and 4, see section 6.1, it is impossible to find a wide distribution of grid points over the domain with zero CLWP for all days. The selected grid points are therefor with cloud free conditions on Day 1 and Day 2. Day 1 and 2 are also the interesting days in this study. Chosen stations are in Aust-Agder (Hynnekleiv, Blåsjø and Sirdal-Sinnes), in Telemark (Skien - Geiteryggen), in Buskerud (Nesbyen-Todokk and Kongsberg Brannstasjon), in Oslo (Oslo-Blindern), in Akershus (Gardermoen and Ås) and in Østfold (Sarpsborg).

Figure 29 show a time series of the averaged surface temperature for 10 grid points for AOD=0, AOD=1.1, AOD=10 and AOD=100, including the surface temperature by Eklima and ERA-Interim. Under the period, the simulated temperature for an AOD≠0 is less than the temperature for an AOD=0, except for the beginning of the simulation. In the beginning of the simulation, the curves are close together but starts to diverge around 6 UTC. As can be understand, the AOD will only make an impact in the presence of solar radiation. On the other hand, during night the temperature difference is still seen, mostly for an AOD=10 and AOD=100. Therefor, the lower temperature for AOD=10 and AOD=100 during day are still influencing the temperature during night.

In the case of comparison with Eklima and ERA-Interim, WRF underestimates the temperature. At Day 1 and 2, comparing AOD=0 and Eklima, a difference of approximately 2 degrees is seen, where ERA-Interim is slightly under Eklima. On Day 3 and 4 the difference is lower, to about 1 degree compared with Eklima, where ERA-Interim slightly under Eklima. On Day 3 and 4 clouds have presence. WRF underestimate therefor the surface temperature more in clear sky conditions. The comparison with Eklima is based on the observation time 12 UTC. A comparison with the maximum temperature of the day, see the bottom right-hand side of figure, the difference is approximately 4 degrees on Day 1, 3 degrees on Day 2, 3.5 degrees on Day 3 and 4 degrees on Day 4. What is also seen, the values of ERA-Interim lies in-between the simulations and Eklima. That is a good indication, since ERA-Interim is an analysis and based on the combination of models and observations.

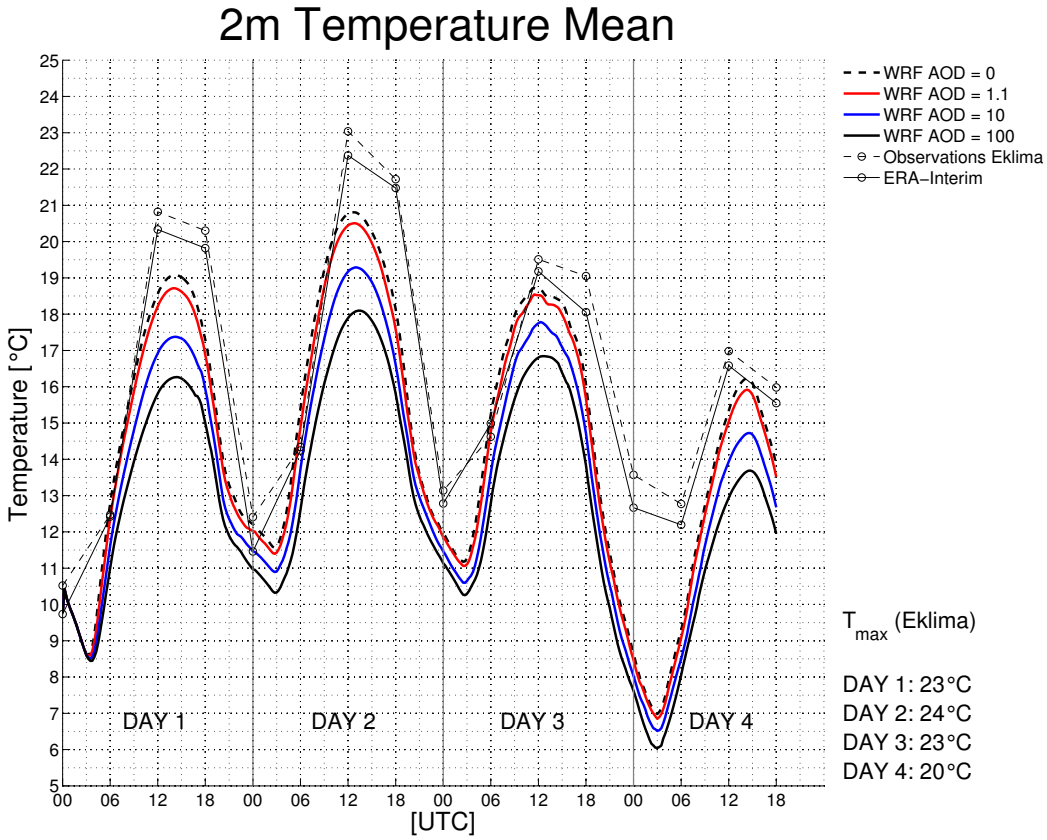

Figure 29: Time series of the averaged surface temperature, 10 stations, for simulations by WRF for an AOD=0, AOD=1.1, AOD=10 and AOD=100 for Day 1 to Day 4. Including synoptic observetions by Eklima and analysis by ERA Interim. Table bottom right-hand side show maximum temperature of the day by Eklima.

Researching the temperature difference for every AOD≠0 with an AOD=0, showed that the maximums are not at the same time as the downward SW-flux has its maximum. The maximum has a tendency to be at 6 UTC and 18 UTC, especially for the difference between an AOD=1.1 and AOD=0. Figure 30 show a time series for the surface temperature difference for each AOD≠0 compared with an AOD=0, including CLWP difference between an AOD=1.1 and AOD=0. Remember on Day 1 and 2 there were clear conditions. As can be seen, on Day 3 and 4, clouds have presence and differences are seen in the CLWP. What is interesting here, looking at the AOD=1.1 and AOD=0 difference on Day 1 and 2, a higher value is seen around 6 and 18. At 6 and 18 the temperature difference is approximately 0.5 degrees comparison to the day time in-between, where it is 0.25 degrees (especially for Day 2). A smaller tendency is seen on Day 3 and 4 during cloudy conditions. For larger AOD, AOD=10 and 100, the same tendency is not seen.
The same time series is plotted for the downward SW-flux difference, see figure 31. The SW-flux difference between AOD=1.1 and AOD=0 is less at

12 than just after 6 and just before 18 on Day 1 and Day 2. The same structure is not seen in the comparison with an AOD=10 and AOD=100.
At 6 and 18 is the time when the sun raises and goes down, respectively. When the sun is lower the path for the penetrating solar radiation trough the layer of an AOD≠0 will be longer. For smaller AOD (~1), the direct radiation through the layer is dominant and for larger AOD (~10), diffuse radiation through the layer is dominant. Therefor, more multiple scattering occur for an AOD=10 and AOD=100 and the tendency will not be seen.

The peak on Day 3 for CLWP, see Figure 30 and 31, corresponds to more CLWP created in simulations by an AOD=0. This leads to a smaller temperature difference between an AOD=1.1 and AOD=0. This indicates further again, the very large importance of CLWP, which is the dominated contributor to the differences in each run.

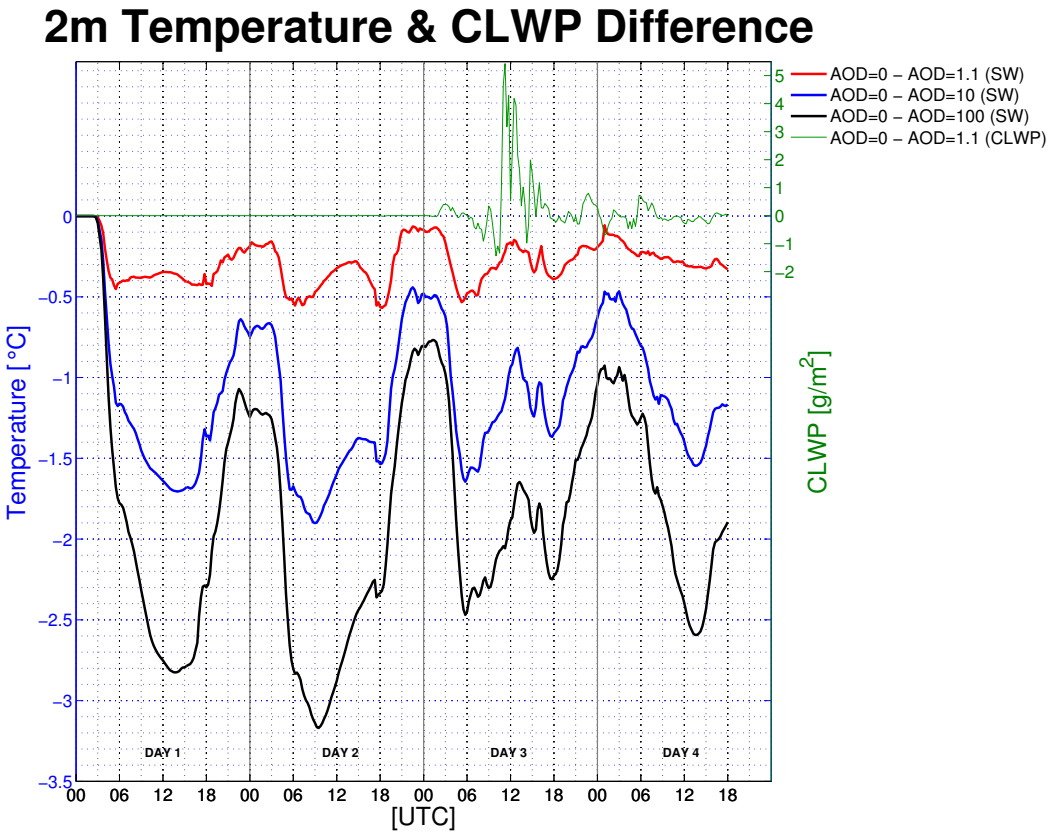

Figure 30: Time series of the averaged surface temperature and cloud liquid water path (CLWP) differences for 10 stations between an AOD=1.1, AOD=10 and AOD=100 with an AOD=0 for Day 1 to Day 4. CLWP is only the difference between an AOD=1.1 and AOD=0.

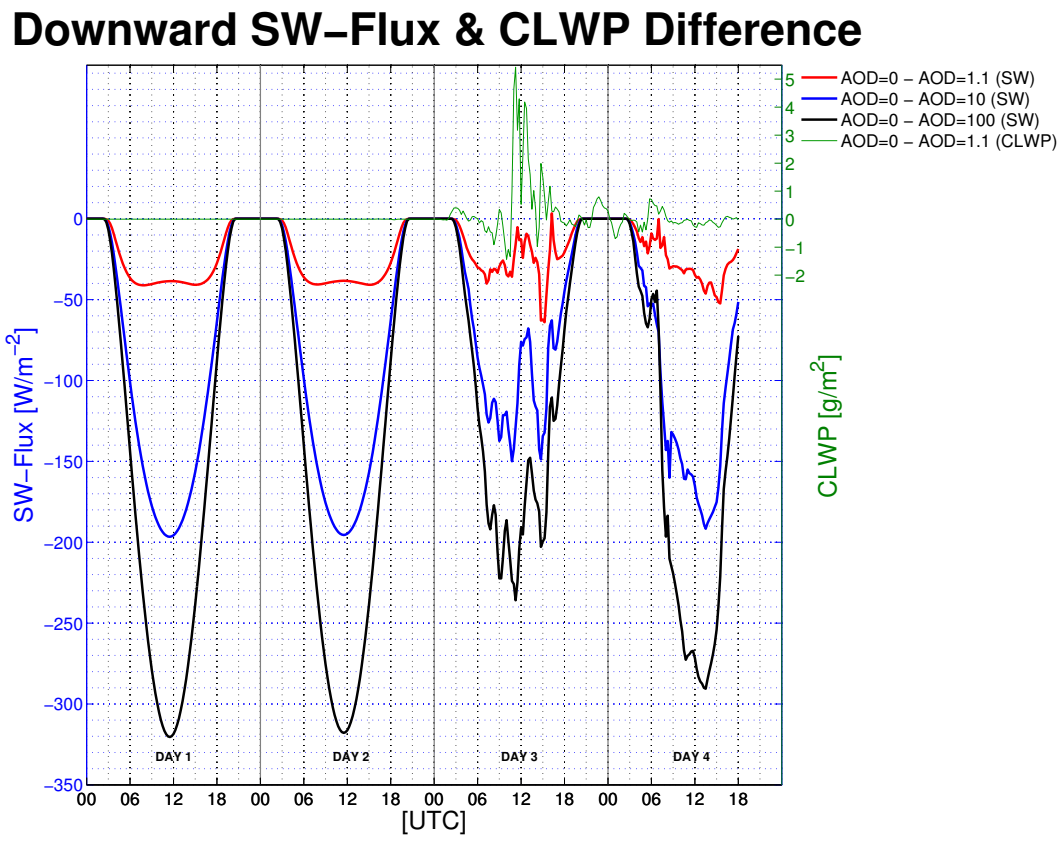

Figure 31: Time series of the averaged downward SW-flux and cloud liquid water path (CLWP) differences for 10 stations between an AOD=1.1, AOD=10 and AOD=100 with an AOD=0 for Day 1 to Day 4. CLWP is only the difference between an AOD=1.1 and AOD=0.

7

CONCLUSION AND FUTURE WORK

In the two concerned periods, events 1 and 2, the smoke most likely originated from wildfires in Quebec, Canada. Recall, event 1 is from June 22 to 27 and event 2 from July 4 to 14, 2013.

• EVENT 1: The source could have been a wildfire east of Manicouagan Lake. The wildfire grew rapidly and developed a very large smoke plume during June 22 and 23, see the large area burned east of Manicouagan Lake in Figure 32. The smoke was detected by OMPS and CALIPSO over the east coast of Canada, east of Newfoundland, on June 23. By CALIPSO measurements, the smoke was detected on an altitude of 4-6km, where also a wind speed of 50 knot was observed. It took approximately 2-3 days to reach Europe, where it was observed south of England on June 25. In England an AOD value of 1.9 was detected by sun photometer operated by AERONET. In the Netherlands a ceilometer observed the smoke on an altitude of 3.5 km, and it had a thickness of 500m.

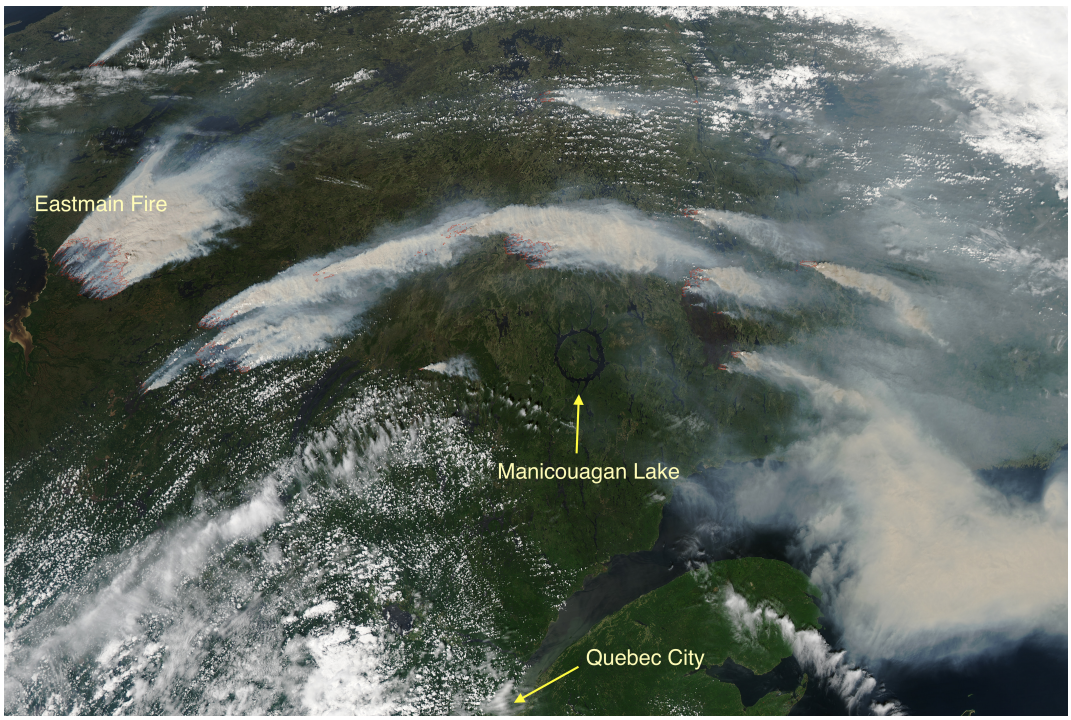

Figure 32: MODIS-Aqua satellite image of wildfires burning in Quebec on July 4, 2013. Detection of hot spots are outlined in red. [30]

• EVENT 2: The source could have been the wildfire in the Eastmain region. The fire is called the Eastmain fire, and on July 4 a large amount of smoke in the combination of pyrocumulonimbus clouds were created, see the fire in Figure 32. The Eastmain fire was the 2nd largest fire since 1959. A trough on a pressure level of 500mb over the Atlantic was seen on July 7. The smoke therefore got transported further up in Europe, to Scandinavia. The smoke was observed over Sweden by MODIS on July 8 with an AOD of 1.5, verified by an operating sun photometer (AERONET). On the same day, ceilometer in Norway detected the smoke plume on an altitude of 3-4 km.

7.1 WRF SIMULATIONS

Differences in surface temperature and downward SW-flux for three different AOD values are presented in Table 2, for clear sky conditions. An AOD of 10 is a typical value of an altostratus cloud and an AOD of 100 can be a very thick nimbostratus. From our simulations using WRF we found that an AOD value of 1.1 decreased the surface temperature by 0.25-0.5 degrees. In this case, the difference in downward SW-flux was approximately 5% of the downward SW-flux with an AOD value of 0. However, this effect was small compared to the one induced by CLWP differences.

Simulation	T	SW
AOD=1.1 vs. AOD=0	0.25-0.5 K	~40W/m^2
AOD=10 vs. AOD=0	1.7-1.9 K	~200W/m^2
AOD=100 vs. AOD=0	2.8-3.2 K	~320W/m^2

Table 2: Difference in surface temperature (T) and downward SW-flux (SW) between AOD=0 with AOD≠0. Simulations with 40x40 domain and a resolution of 15x15 km for clear sky conditions.

By using the same method as applied in this thesis, it would be interesting to see the surface temperature impact in other SW radiation schemes in WRF. Since any model has its own weaknesses and is not perfect, it would be worthwhile to compare with results from other numerical weather prediction models.

BIBLIOGRAPHY

[1] Acker, J. G., and G. Leptoukh (2007) Online Analysis Enhances Use of NASA Earth Science Data. Eos, *Transactions American Union*, Vol. 88, No. 2, pages 14 and 17.

[2] Boucher, O., D. Randall, P. Artaxo, C. Bretherton, G. Feingold, P. Forster, V.-M. Kerminen, Y. Kondo, H. Liao, U. Lohmann, P. Rasch, S.K. Satheesh, S. Sherwood, B. Stevens and X.Y. Zhang (2013) *Clouds and Aerosols. In: Climate Change 2013: The Physical Science Basis*. Contribution of Working Group I to the Fifth Assessment Report of the Intergovernmental Panel on Climate Change [Stocker, T.F., D. Qin, G.-K. Plattner, M. Tignor, S.K. Allen, J. Boschung, A. Nauels, Y. Xia, V. Bex and P.M. Midgley (eds.)]. Cambridge, United Kingdom and New York, NY, USA, Cambridge University Press.

[3] Briegleb, B. P. (1992) Delta-Eddington approximation for solar radiation in the NCAR community climate model. *Journal of Geophysical Research*, Vol. 97, NO. D7, pages 7603-7612.

[4] California Regional Weather Server (2014), San Francisco State University [Internet]. Available from: http://squall.sfsu.edu [Accessed 27 April 2014].

[5] Canadian Interagency Forest Fire Centre Inc. National Wildland Fire Situation Report (Sep 11, 2013) [Internet]. Available from: http://www.ciffc.ca/firewire/current.php [Accessed 10 April, 2014].

[6] Climate Denial Crock of the Week with Peter Sinclair (2014) in "Dr. Jeff Masters: Quebec Fire Second Largest in Record" [Internet]. Available from: http://climatecrocks.com/2013/07/14/dr-jeff-masters-quebec-fire-second-largest-in-record/ (accessed April 15, 2014).

[7] Natural Resources Canada (2014), Canadian Wildland Fire Information System [Internet]. Available from: http://cwfis.cfs.nrcan.gc.ca/report/archives [Accessed 10 April 2014].

[8] CBC News (2014) in "Smoke causes partial evacuation of Quebec Cree community" [Internet]. Available from: http://www.cbc.ca/news/canada/north/smoke-causes-partial-evacuation-of-quebec-cree-community-1.1331591 (accessed April 15, 2014).

[9] Cess, R. D. (1985) Nuclear war: Illustrative effects of atmospheric smoke and dust upon solar radiation. *Climate Change*, 7, 237-251.

[10] Coakley, J. A., R. D. Cess, and F. B. Yurevich (1983) *The effect of tropospheric aerosols on the Earth's radiation budget: A parameterization for climate models*. Journal of the Atmospheric Sciences, 40, 116-138.

[11] Collins, W. D., P. J. Rasch, B. A. Boville, J. J. Hack, J. R. McCaa, D. L. Williamson, J.T. Kiehl, B. Briegleb, C. Bitz, S. Lin, M. Zhang and Y. Dai (2004) Description of the NCAR community atmosphere model (CAM 3.0). *NCAR Technical Note*, NCAR/TN-464+STR, 214pp.

[12] Draxler, R.R. and G.D. Rolph (2013) HYSPLIT (HYbrid Single-Particle Lagrangian Integrated Trajectory), NOAA Air Resources Laboratory, College Park, MD, Model access via NOAA ARL READY Website [Internet]. Available from: http://www.arl.noaa.gov/HYSPLIT.php [Accessed 15 May 2014].

[13] ECMWF (2014), ERA-Interim [Internet]. Available from: http://data-portal.ecmwf.int/data/d/interim_daily/ [Accessed 16 January 2014].

[14] Eumetrain (2014) [Internet]. Available from: http://www.eumetrain.org [Accessed 27 April 2014].

[15] Hansen, J., M. Sato, L. Nazarenko, R. Ruedy, A. Lacis, D. Koch, I. Tegen, T. Hall, D. Shindell, B. Santer, P. Stone, T. Novakov, L. Thomason, R. Wang, Y. Wang, D. Jacob, S. Hollandsworth, L. Bishop, J. Logan, A. Thompson, R. Stolarski, J. Lean, R. Willson, S. Levitus, J. Antonov, N. Rayner, D. Parker and J. Christy (2002) Climate forcings in Goddard Institute for Space Studies SI2000 simulations. *Journal of Geophysical Research*, 107(D18), 4347, doi:10.1029/2001JD001143.

[16] Janhäll, S., Andreae M. O. and Pöschl U (2010) Biomass burning aerosol emissions from vegetation fires: particle number and mass emission factors and size distributions. *Atmospheric Chemistry Physics*, 10, 1427-1439.

[17] JENOPTIK AG (2014), Meteorology and Environmental Sensing, Ceilometer CHM 15k [Internet]. Available from: http://www.jenoptik.com/en_50377_chm_15k [Accessed 26 March 2014].

[18] Karasiński, G., A. E. Kardaś, K. Markowicz, S.P. Malinowski, T. Stacewicz, K. Stelmaszczyk, S. Chudzyński, W. Skubiszak, M. Posyniak, A.K. Jagodnicka, C. Hochhertz, and L. Woeste (2007) LIDAR investigation of properties of atmospheric aerosol. *The European Physical Journal Special Topics 144*, 129-138.

[19] KNMI (2014), Royal Netherlands Meteorological Institute [Internet] in "Rookpluimen uit Amerika boven Europa". Available from: http://www.knmi.nl/cms/content/113942/rookpluimen_uit_amerika_boven_europa (Translated to english) [Accessed 14 April 2014].

[20] Levy, R. C., L. A. Remer, R. G. Kleidman, S. Mattoo, C. Ichoku, R. Kahn, and T. F. Eck (2010) Global evaluation of the Collection 5 MODIS dark-target aerosol products over land. *Atmospheric Chemistry and Physics*, 10, 10399-10420.

[21] Liou, K. N. (2002). *An Introduction to Atmospheric Radiation, 2nd Edition*. Academic Press.

[22] Lohmann, U. and J. Feichter (2005) Global indirect aerosol effects: a review. *Atmospheric Chemistry and Physics*, 5, 715-737, doi:10.5194/acp-5-715-2005.

[23] macc (2014), Monotoring atmospheric composition & climate in "Canadian smoke spreading over Europe" [Internet]. Available from: https://www.gmes-atmosphere.eu/news/canada_smoke/ [Accessed 28 April 2014].

[24] NASA (2014a), AErosol RObotic NETwork (AERONET),NASA and PHOTONS [Internet]. Available from: http://aeronet.gsfc.nasa.gov/new_web/index.html [Accessed 1 June 2014].

[25] NASA (2014b), EARTHDATA, Aerosol Index [Internet]. Available from: http://disc.sci.gsfc.nasa.gov/data-holdings/PIP/aerosol_index.shtml [Accessed 28 May 2014].

[26] NASA (2014c), Goddard Earth Sciences Data and Information Services Center, Giovanni, MODIS Terra and Aqua Daily Level-3 Data [Internet]. Available from: http://gdata1.sci.gsfc.nasa.gov/daac-bin/G3/gui.cgi?instance_id=MODIS_DAILY_L3 [Accessed 15 May 2014].

[27] NASA (2014d), NASA Earth Observatory [Internet]. Available from: http://neo.sci.gsfc.nasa.gov/view.php?datasetId=MYDAL2_M_AER_OD [Accessed 6 June 2014].

[28] NASA (2014e), NASA Earth Observatory in " A Vertical View of Wildfire Smoke as it Heads to Sea : Image of the Day" [Internet]. Available from: http://earthobservatory.nasa.gov/IOTD/view.php?id=81520 [Accessed 14 April 2014].

[29] NASA (2014f), NASA Earth Observatory in "Wildfires Smoke Crosses the Atlantic : Natural Hazards" [Internet]. Available from:

http://earthobservatory.nasa.gov/NaturalHazards/view.php?id=81500 [Accessed 14 April 2014].

[30] NASA (2014g), NASA Earth Observatory in "Smoke and Wildfires in Quebec : Natural Hazards" [Internet]. Available from: http://earthobservatory.nasa.gov/NaturalHazards/view.php?id=81613 [Accessed 12 June 2014].

[31] NASA (2014h), OMPS, Suomi National Polar-orbiting Partnership [Internet]. Available from: http://ozoneaq.gsfc.nasa.gov/omps/ [Accessed 13 April 2014]

[32] NERC Satellite Receiving Station (2014), Dundee University, Scotland [Internet]. Available from: http://www.sat.dundee.ac.uk/ [Accessed 7 June 2014].

[33] Norwegian Meteorological Institute (2014), eKlima [Internet]. Available from: http://sharki.oslo.dnmi.no/portal/page?_pageid=73,39035,73_39049&_dad=portal &_schema=PORTAL [Accessed 16 January 2014].

[34] O'Neill, N. T., T. F. Eck, A. Smirnov, B. N. Holben, and S. Thulasiraman (2003) Spectral discrimination of coarse and fine mode optical depth, *Journal Geophysical Research*, Volume 108, No. D17, 4559-4573, 10.1029/2002JD002975.

[35] PyroCb (2014a) by Cooperative Institute for Meteorological Satellite Studies in "Large fire in southeastern Quebec" [Internet]. Available from: https://pyrocb.ssec.wisc.edu/archives/89 [Accessed 28 April 2014].

[36] PyroCb (2014b) by Cooperative Institute for Meteorological Satellite Studies in "Fires in western Quebec" [Internet]. Available from: http://pyrocb.ssec.wisc.edu/archives/136 [Accessed 20 April 2014].

[37] Reid, J. S., R. Koppmann, T. F. Eck and D. P. Eleuterio (2005) A review of biomass burning emissions part II: intensive physical properties of biomass burning particles. *Atmospheric Chemistry Physics*, 5, 799-825.

[38] Remer, L. A., Y. J. Kaufman, et al. (2005). *The MODIS aerosol algorithm, products, and validation*. Journal of the Atmospheric Sciences 62(4): 947-973.

[39] RMI (2014), The Royal Meteorological Institute of Belgium [Internet]. Available from: http://www.meteo.be/meteo/view/fr/10671878-De+la+fumee+americaine+en+Belgique.html (Translated to english) [Accessed 7 June 2014]

[40] Royal Netherlands Meteorological Institute (2014), Earlinet, Lidar [Internet]. Available from: http://www.knmi.nl/samenw/earlinet/quicklookpages/lidar/Cabauw/ [Accessed 15 April 2014].

[41] Seinfeld, J.H. and S.N., Pandis (1998). *Atmospheric Chemistry and Physics: From Air Pollution to Climate Change, 2nd Edition*. John Wiley & Sons, Inc.

[42] Skamarock, W. C., J. B. Klemp, J. Dudhia, D. O. Gill, D. M. Barker, M. G Duda, X. Huang, W. Wang and J.G. Powers (2008) A description of the advanced research WRF version 3. *NCAR Technical Note*, NCAR/TN-475+STR, 113pp.

[43] Torres, O., P.K., Bhartia, J. R., Herman, Z., Ahmad and J. Gleason (1998). *Derivation of aerosol properties from satellite measurements of backscattered ultraviolet radiation: Theoretical basis*. Journal of Geophysical Research, VOL. 103, NO. D14, pages 17, 099-17, 110.

[44] Urbanski, S. P., W. M. Hao and S. Baker (2009) Chemical composition of wildland fire emissions. In: Bytnerowicz, A., M. Arbaugh, A. Riebau, C. Andersen, eds. *Developments in environmental science Volume 8: Wildland fires and air pollution*. The Netherlands, Elsevier, pp. 79-107.

[45] Wallace, J.M. and P.V, Hobbs (2006). *Atmospheric Science: An Introductory Survey, 2nd Edition*. Academic Press.

[46] Winker, D. M., W. H. Hunt and M. J. McGill (2007) Initial performance assessment of CALIOP. *Geophysical Research Letters*, VOL. 34, L19803, doi:10.1029/2007GL030135.

[47] WRF ARW OnLine Tutorial (2014) [Internet]. Available from: http://www2.mmm.ucar.edu/wrf/OnLineTutorial/CASES/NestRuns/ndown.htm [Accessed 19 January 2014].